frontiers | Frontiers in Climate

TYPE Original Research
PUBLISHED 01 July 2025
DOI 10.3389/fclim.2025.1592626

OPEN ACCESS

EDITED BY
Ben W. Kolosz,
University of Hull, United Kingdom

REVIEWED BY
Edson Campanhola Bortoluzzi,
The University of Passo Fundo, Brazil
Jiten Pattnaik,
University of Johannesburg, South Africa

*CORRESPONDENCE
Zivi R. Schaffer
✉ zivischaffer@trentu.ca

RECEIVED 12 March 2025
ACCEPTED 02 June 2025
PUBLISHED 01 July 2025

CITATION
Schaffer ZR, Rausis K, Power IM and Paulo C (2025) Enhanced weathering of kimberlite residues in a field experiment: implications for carbon removal quantification and mine waste valorization. *Front. Clim.* 7:1592626.
doi: 10.3389/fclim.2025.1592626

Enhanced weathering of kimberlite residues in a field experiment: implications for carbon removal quantification and mine waste valorization

Zivi R. Schaffer*, Kwon Rausis, Ian M. Power and Carlos Paulo

Trent School of the Environment, Trent University, Peterborough, ON, Canada

Scaling up enhanced rock weathering (ERW) will require gigatonnes of suitable rock, which could include mine wastes such as the estimated 3.9 Gt of kimberlite residues from historic diamond mining. Here, we conducted meter-scale field experiments (2021–2023) in Ontario, Canada, to assess fine processed kimberlite residues for ERW and test carbon-based methods for CO_2 removal (CDR) quantification, including CO_2 fluxes, and measurements of soil and porewater inorganic carbon. A control plot consisted of local calcareous (16.1 wt.% calcite) Brunisolic soil to assess background weathering rates. Two soil plots were amended with 20 and 40 kg of kimberlite residues from the Gahcho Kué Diamond Mine (Northwest Territories, Canada) that contained 30.2 wt.% lizardite [$Mg_3Si_2O_5(OH)_4$], 9.4 wt.% forsterite (Mg_2SiO_4), and 1.9 wt.% calcite ($CaCO_3$). Coinciding with increases in Mg and Si, dissolved inorganic carbon increased in porewaters with kimberlite dosage (amended: 64–118 mg C/L, control: 56 ± 14 mg C/L), demonstrating CO_2 solubility trapping. Water chemistry data, coupled with a water budget derived from weather and soil moisture data, were used to determine CDR rates. The removal rates by the kimberlite residues were up to 1.4 t CO_2/ha over 3 years calculated using porewater inorganic carbon loadings, with Ca and Si loadings allowing for partitioning of rates into removal contributions by kimberlite-derived carbonate weathering (~75%) and silicate weathering (~25%), respectively. CO_2 fluxes and soil inorganic carbon proved ineffective for CDR quantification, given the high effluxes due to soil respiration and high and variable carbonate content of the soils, respectively. Stable carbon isotope data demonstrated that the removed CO_2 was derived from organic carbon, suppressing soil CO_2 effluxes to the atmosphere. This study has implications for repurposing environmentally safe mine wastes for ERW with the potential to reduce net CO_2 emissions and storage and remediation costs in the mining industry. We highlight similarities between kimberlite residues and basalt fines, a common quarry by-product used in ERW, advocating for the use of processed rock from current and legacy mining operations for CDR. Further, our CDR monitoring approaches that effectively distinguish between silicate and carbonate weathering may be utilized in other ERW applications.

KEYWORDS

kimberlite, mine waste, enhanced weathering, CO_2 removal, carbon accounting, field experiment

1 Introduction

The ongoing failure to achieve greenhouse gas (GHG) reduction targets necessitates the adoption of negative emissions technologies (NETs) that remove carbon dioxide (CO_2) from the atmosphere (UNFCCC, 2015; Hoegh-Guldberg et al., 2018). Concurrently, the metals and mining industry generates ~100 Gt/year of solid waste and contributes 4–7% to global GHG emissions (Wani et al., 2022; Weiler et al., 2024). While the industry aims to reduce emissions through electrification, it can also benefit from implementing NETs that have robust carbon accounting measures to strengthen efforts to decarbonize their operations (Power et al., 2024).

CO_2 mineralization of processed kimberlite from diamond mining has been documented (Rollo and Jamieson, 2006; Lockhart et al., 2024) and previously estimated using quantitative mineralogical analyses supported by stable carbon isotope data (Wilson et al., 2009, 2011) and investigated using various laboratory experiments (Paulo et al., 2021; Stubbs et al., 2022; Jones et al., 2023; Wang et al., 2024). Despite mineralogical suitability [e.g., abundance of lizardite ($Mg_3Si_2O_5(OH)_4$)], the rate of fine processed kimberlite carbonation in impoundments is slow (e.g., Venetia Diamond Mine, South Africa: 470 g CO_2/m^2/year, Diavik Diamond Mine, Canada: 375–510 g CO_2/m^2/year; Paulo et al., 2023) relative to the pace at which industrial CO_2 emissions are produced. Further, tailings impoundments are designed to minimize weathering, and thus, prevent reactions with atmospheric CO_2. Consequently, there have been recommendations to modify tailings management practices to improve CO_2 ingress and facilitate CO_2 mineralization (e.g., reduce water content in tailing ponds; Power et al., 2013a, 2013b; Wilson et al., 2014). Similar adjustments to mine waste management could include spreading wastes over mine sites or adjacent land to increase atmospheric exposure (Power et al., 2024).

Enhanced rock weathering (ERW) has emerged as a potentially viable and scalable NET that involves spreading silicate rock powders to accelerate the weathering and dissolution of target minerals [e.g., lizardite and forsterite (Mg_2SiO_4)], an approach that is in stark contrast to mine waste storage. Power et al. (2024) describe the potential roles the mining industry can play in advancing ERW at their sites and as a supplier of rock powder. ERW has potential for a global impact on CO_2 mitigation if the vast abundances of suitable rock can be mined and supplied (Moosdorf et al., 2014; Renforth et al., 2015; Goll et al., 2021; Paulo et al., 2021; Stubbs et al., 2022). Recent ERW field trials have primarily applied crushed basalt to agricultural fields (Larkin et al., 2022; Guo et al., 2023; Kantola et al., 2023); however, quantifying carbon storage derived from the weathering of other rock types is needed to progress ERW. Furthermore, environmental variabilities (e.g., climatic variance and soil types) prevent the development of a one-size-fits-all method, requiring tailored approaches that partition soil CO_2 consumption rates from feedstock weathering contributions and considers carbonate weathering (Almaraz et al., 2022). Still, the benefits of spreading silicate rock powders encourages research and implementation of ERW as co-benefits may include increased nutrient availability and plant growth and potentially aid mine closure remediation (Schuiling and Krijgsman, 2006; Moosdorf et al., 2014; Gunnarsen et al., 2023).

This study aimed to advance the utilization of mine wastes for ERW by defining a measurable approach for CO_2 removal quantification and introducing a significant contribution to the circular economy by repurposing mine wastes from diamond mines, an industrial waste. The goals of this study were to (1) assess the suitability of kimberlite as a soil amendment for CDR, (2) quantify CO_2 removal by kimberlite residues amended to soil field plots, and (3) evaluate several approaches for monitoring carbon removal. To achieve these goals, fine processed kimberlite residues from Gahcho Kué Diamond Mine (Northwest Territories, Canada) were characterized to determine geochemical, mineralogical, and physical properties in the context of ERW applications, followed by batch leaching experiments for an initial assessment of reactivity and element release. Square-meter soil plots amended with varying dosages of kimberlite residues and a soil control were monitored for 3 years as an ERW field experiment in Southern Ontario, Canada. Best practices for monitoring carbon removal in climates similar to this field site consisted of coupling carbon-based measurements in soil waters with cation loadings determined via a water balance derived from hydrological parameters.

2 Materials

2.1 Kimberlite residue acquisition

As part of De Beers' Project CarbonVault, approximately 300 kg of fine processed kimberlite (FPK) were transported as a slurry from Gahcho Kué Diamond Mine to Trent University in 2020. The mine is an open pit operation located in the Northwest Territories, Canada (63°N 26′ 29.5″, 109°W 10′ 36″) that extracts diamond-bearing kimberlite from four main pipes emplaced into the Archaeon Slave Craton granitoids (Hetman et al., 2004). In addition to detailed characterization, these residues were used for the batch leaches with CO_2 and ERW field experiment.

In addition, fine kimberlite residues were obtained from the Jwaneng and Orapa ($n = 12$) diamond mines in Botswana, and Voorspoed ($n = 3$) and Venetia ($n = 34$) Diamond Mine in South Africa. These residues were only analyzed by X-ray fluorescence spectroscopy to compare their geochemical composition to the Gahcho Kué residues.

2.2 Residue and soil characterization

The Gahcho Kué (GK) kimberlite residues and local field soil were analyzed for their mineralogical and geochemical composition, and physical characteristics. Quantitative mineralogical data were obtained by Rietveld refinement of powder X-ray diffraction (XRD) data analyzed using a Bruker D8 Advance and Bruker D2 Phaser θ-θ X-ray diffractometer. Geochemical data were determined using X-ray fluorescence (XRF) spectroscopy (major oxides), and inductively coupled plasma optical emission spectroscopy (ICP-OES; trace elements) after samples were prepared using a 4-acid digestion. Additional chemical characterization included total inorganic carbon (TIC) content of the residues measured via carbon coulometry, and total cation exchange capacity (CEC) measured by ICP-OES analysis of leachate extractions. Specific surface areas (SSA) were determined using the Brunauer–Emmett–Teller (BET) method of N_2 adsorption (Brunauer et al., 1938), and particle size distribution (PSD) were determined using a Horiba LA-950 V2 laser scattering particle size distribution analyzer. Detailed analytical methods with detection limits and analytical errors are provided in the Supplementary Methods.

Three soil core samples (98 cm^3) were collected at the ERW field experiment site with each soil profile divided into the surface (0–5 cm), middle (5–15 cm), and bottom (15–30 cm) fractions (Supplementary Table S1). Samples were dried under ambient conditions, disaggregated, and sieved (<2 mm) before characterization of geochemical and physical properties. The bulk density of the soil weatherable fraction was determined by water displacement of an undisturbed soil core, with the >2 mm mass fraction and organic matter content subtracted from the total soil mass. Bulk surface samples were used for the batch leaching experiment.

3 Site description

Field experiments were conducted from June 2021 to October 2023 on the Trent University Symons Campus in Peterborough, Ontario, Canada (44°N 21′ 0″, 78°W 17′ 24″) using homogenized fine processed kimberlite from the Gahcho Kué Diamond Mine applied to local Brunisolic soil plots. This outdoor experimental site had an elevation of ~230 MAMSL and featured a relatively flat terrain (~2° slope). The soil was classified as sandy loam, exhibiting good drainage and low potential for runoff or accumulation. Peterborough has a humid continental climate with the average warmest temperature in July (26.6°C) and coldest average temperature in January (−12.8°C), and an average annual precipitation of 840 mm, ~19% of which falls as snow (ECCC, 2021). Weather data, including rainfall, total precipitation, and air temperature were recorded quarter-hourly at the Trent Climate Station, 1 km south of the study site. Although this site had a history of agriculture (pre-20th century; Jones et al., 2002), it was currently undisturbed buffer land with the nearest agricultural activity ~500 m east.

4 Methods

4.1 Batch leaches with CO_2

Batch leaches were conducted as an initial assessment of cation release that may occur in the field experiment. This method was modified from the tests by Paulo et al. (2021) and does not mimic field conditions (e.g., high liquid-to-solid ratio and CO_2 concentration). Instead, these leaches aimed to determine an upper potential for leachate concentrations under circumneutral to slightly acidic conditions and were used to determine cation indicators for mineral dissolution to be used in field data analysis, and assess potential metal (e.g., Ni and Cr) leaching.

Kimberlite residues and soils were mixed for a total mass of 250 mg, with varying kimberlite concentrations (0, 0.5, 1, 5, 10, 15, 25, 50, 75, and 100 wt.%), and are henceforth referred to as 0GK, 0.5GK, 1GK, 5GK, 10GK, 15GK, 25GK, 50GK, 75GK, and 100GK. Aliquots of soil-kimberlite mixtures (e.g., 25 wt.% soil and 75 wt.% kimberlite is labeled as 75GK) were added to 100 mL of deionized water (18.2 MΩ·cm). The experiment consisted of triplicate polyethylene flasks for control soil (0GK) and kimberlite residues (100GK), one of deionized water only, and one flask each for the remaining mixtures for a total of 15 flasks. A ThermoScientific™ CO_2 Resistant Shaker table set to 150 rpm was used to mix the suspensions inside a ThermoScientific™ HERAcell VIOS 160i CO_2 incubator (35°C, 10% CO_2, 21.9% O_2) at nearly 100% relative humidity. Uncapped flasks were mixed inside the chamber for 2 weeks. Upon completion of the batch leach, pH was measured, and leachates were filtered (0.22 μm) into 50 mL plastic centrifuge tubes and acidified (2% v/v ultrapure HNO_3, Aristar®, UK). Water samples were stored at 4°C prior to cation analysis by inductively coupled plasma mass spectrometry (ICP-MS). Principal component analysis of the batch leach data was completed using OriginPro (v. 9.9).

Aliquots (5.0 g) of kimberlite residues and soils (0, 0.5, 1, 5, 10, 25, 50, and 100 wt. % kimberlite) were analyzed for geochemical compositions by XRF and ICP-OES to determine the percentage of cations leached from the solids. In 2.5 g increments, the mixtures were micronized for 7 min in anhydrous ethanol using a McCrone Micronizing Mill and left to dry overnight in a fume hood prior to analysis.

4.2 ERW field experiment

4.2.1 Design and setup

Field plots (1 m^2) were used to monitor the weathering of Gahcho Kué residues applied to soil and determine the CDR achieved over three monitoring periods—extrapolated to 3 years. Three circular soil plots (1 m^2) were created in June 2021, orientated so that ~2 m of space separated each plot possessing similar soil and vegetation characteristics in each (Figure 1A) within a fenced enclosure (Figure 1B). In each plot, a SoilMoisture 1900 L 18-B02M2 Near Surface porewater sampler (46 cm length) and TEROS 12 soil moisture probe (METER Group Inc.) were installed at 15 and 30 cm depths (Figure 2). The probes measured soil volumetric water content (m^3/m^3) and temperature (°C) every 15 min, recording values on an on-site ZL6 data logger (METER Group Inc.). A soil gas lance (BGLD-300; METER Group Inc.) was used to sample soil pore gas to measure CO_2 concentrations at 20 cm depth (Figure 2). All holes created during instrument installation were backfilled with a ~1:1 slurry of the excavated soil and deionized water.

Vegetation was removed from the plots, tilling the soil lightly with a garden cultivator to create a loose soil layer to ease amendment mixing to a depth of ~3 cm. One plot was used as a control to assess natural background weathering (Figure 1C). The other two plots were amended with 10 and 20 kg of Gahcho Kué fine kimberlite residues in June 2021; however, in June 2022, an additional 30 kg of kimberlite residues was added to the 10 kg plot to assess a repeated application of the residues (Figure 1D). The amended plots are denoted K10+30 and K20, respectively. Some ERW field trials reapply amendments annually (Larkin et al., 2022; Beerling et al., 2024) to sustain or enhance CDR, improve CDR signal detection, or assess environmental impacts from multiple applications. The K20 plot demonstrated a single high dosage (200 t/ha), while the K10+30 (100 + 300 t/ha) provided insight into the impact repeated amendments may have on CDR efficiency, metal loading, and porewater saturation. The kimberlite residues were applied by hand, mixing into the loosened soil. A polyvinyl chloride (PVC) collar (ø = 20 cm) was inserted into each plot after amendment for CO_2 flux measurements.

The aforementioned equipment was first removed in October 2021 for the winter, and the plots left unmonitored for 6 months

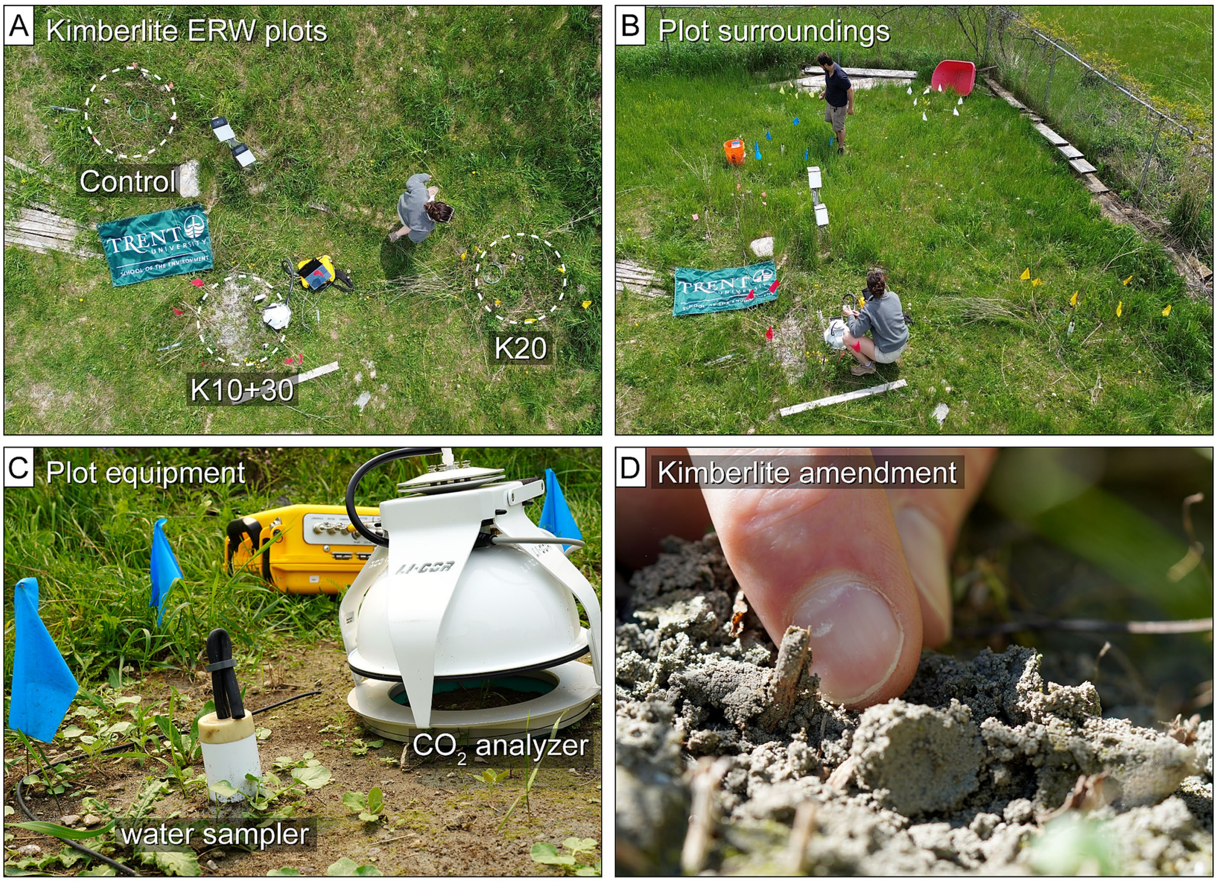

FIGURE 1
Orientation of the three square-meter plots, with two different application rates of kimberlite residues (K10+30: 10 + 30 kg/m^2; K20: 20 kg/m^2) and a control **(A)**. Outdoor experimental area at Trent University **(B)**. The control plot showing one of two water samplers and the CO$_2$ analyzer measuring CO$_2$ surface fluxes **(C)**. Fine processed kimberlite amendment on the K10+30 plot after reamendment **(D)**.

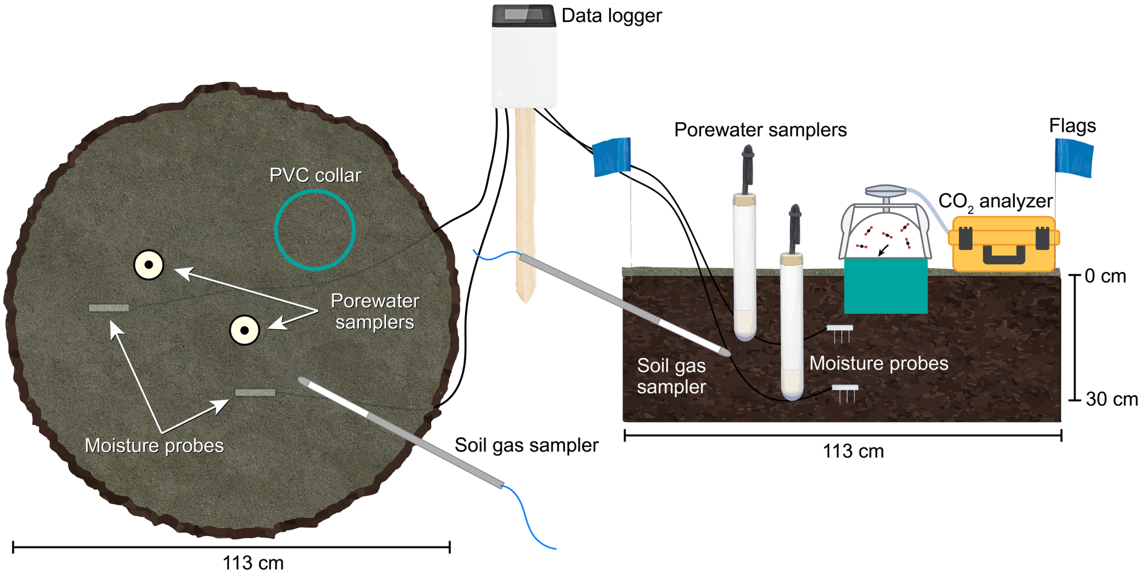

FIGURE 2
Experimental setup for field plots that were equipped with porewater samplers at 15 and 30 cm depths and a soil gas sampler at 20 cm depth. TEROS 12 moisture probes were installed at 15 and 30 cm depths, recording data onto a ZL6 data logger located outside of the plot. A 20 cm diameter PVC collar with a 2 cm offset was used for CO$_2$ flux measurements using a LI-COR survey chamber and LI-8100A CO$_2$ analyzer.

between November 2021 and May 2022 upon which equipment was reinstalled and monitoring continued uninterrupted for the next 16 months (to end of September 2023). The experiment was divided into three monitoring periods: the first (June 2021–October 2021), second (May 2022–December 2022), and third monitoring period (January 2023–September 2023), concluding after ~3 years.

4.2.2 CO_2 fluxes and pore gas measurements

The PVC collars were inserted into soils to a depth of 14 cm, leaving a 2 cm offset; however, over time this offset increased to ~5 cm from natural compaction of the soil and was accounted for during measurements. CO_2 fluxes were measured daily for 2 weeks immediately following kimberlite amendments using a LI-8100 soil CO_2 flux system equipped with a survey chamber (LI-COR, Lincoln, Nebraska, USA), and once weekly throughout each monitoring period. This instrument measures the diffusion rate of CO_2 (μmol/m^2/s) over a programmed period of 3 min. The control plot was used to compare natural fluxes to the amended soil fluxes, where negative values indicated CO_2 drawdown and positive indicated CO_2 efflux. These methods and data analysis are provided in the Supplementary Methods.

Soil pore gas was sampled at 20 cm depths using a 60 mL syringe to draw pore gas using a soil gas lance and through a Vaisala CARBOCAP® Carbon Dioxide Probe GMP251 (0–20% CO_2) that measures the CO_2 concentrations that are displayed using an MI70 indicator. Values were recorded bi-monthly with a ± 0.2% accuracy in each reading in a 0–8% CO_2 range.

4.2.3 Water sampling

The plots were initially wetted with 20 L of deionized water in 5 L increments over 2 h to test water sampler installation and to allow instruments to settle into the surrounding soil. A hand pump with pressure gauge was used to achieve a vacuum of at least 70 kPa in each of the surface porewater samplers, allowing porewater to be drawn into the porous ceramic cup at the base of the sampler. Samplers were pumped weekly, or following a rain event, for opportunistic sample collection; however, sample collection was limited during dry periods such as August 2021. From December 2022 to March 2023, which was a particularly mild winter, water samples were collected during periods of snow melt.

pH was measured immediately after sampling using a ThermoScientific Orion 4-Star pH/ISE meter that was calibrated daily. Samples were filtered (0.22 μm) into 50 mL plastic centrifuge tubes with aliquots of 30 mL being acidified (2% v/v ultrapure HNO_3, Aristar®, UK) for major and trace element analysis. All non-acidified samples were analyzed for alkalinity and dissolved inorganic carbon (DIC), while only select samples were analyzed for major anions ($n \geq 4$ per monitoring period) and stable carbon and oxygen isotopes ($n = 2$). Saturation indices of relevant mineral phases were determined using PHREEQC Interactive v. 3.4.0 (Parkhurst and Appelo, 2013) with the carbfix.dat database (Voigt et al., 2018). Samples were stored at 4°C prior to analysis. One way ANOVA ($p < 0.05$) was used to compare the three plots in mean DIC, alkalinity, and pH at 15 and 30 cm, coupled with Tukey's post-hoc test for pairwise comparisons. Detailed analytical methods are provided in the Supplementary Methods.

4.2.4 Soil sampling

To determine pedogenic carbonate precipitation in the experiment plots, triplicate soil cores were sampled using a soil core sampler down to ~25 cm in each plot in December 2022 and November 2023. Soil cores were divided into 2–5 cm increments upon collection, dried in a fume hood, and homogenized prior to storage. Dried soils at each depth were micronized (~1 g) and ~100 mg aliquots were analyzed for TIC.

5 Results

5.1 Soil and residue characterization

Soils at the study site were classified as an Orthic Melanic Brunisol, characterized by high organic content ($LOI_{1000^\circ C}$: 16.8%), calcareous parent material, and thus a neutral pH (Smith et al., 2011). These sandy loam soils had a D80 particle size of 166–339 μm, a specific surface area of 3.4 m^2/g, and a CEC of 11.7 ± 3.3 cmol/kg (Table 1). The mineralogical assemblage was dominated by quartz (SiO_2; 30.7 wt.%), albite ($NaAlSi_3O_8$; 23.4 wt.%), microcline ($KAlSi_3O_8$; 23.4 wt.%), and calcite ($CaCO_3$; 16.1 wt.%), with lesser abundances of ferro-pargasite [$NaCa_2(Fe^{2+}{}_4Al)(Si_6Al_2)O_{22}(OH)_2$; 6.5 wt.%; Table 1]. Oxide abundances were mainly composed of SiO_2 (53.3 wt.%), with lesser amounts of Al_2O_3 (10.7 wt.%), CaO (8.9 wt.%), Fe_2O_3 (4.0 wt.%), K_2O (2.1 wt.%), Na_2O (1.9 wt.%), and MgO (1.4 wt.%), and remaining oxide abundances being <1 wt.%.

The Gahcho Kué residues had a D80 particle size of 175 μm, a specific surface area of 20.6 m^2/g, and a CEC of 6.0±0.1 cmol/kg (Table 1). The kimberlite residues were mainly composed of SiO_2 (42.9 wt.%) and MgO (27.1 wt.%), and lower percentages of Fe_2O_3 (7.0 wt.%), Al_2O_3 (5.1 wt.%), CaO (4.0 wt.%), K_2O (2.5 wt.%), with

TABLE 1 Physical, geochemical, and mineralogical characteristics of fine processed kimberlite (FPK) and surface soil ($n = 3$).

Physiochemical parameters	Fine processed kimberlite	Soil
SSA (m^2/g)	20.6	3.4
TIC (%)	0.25 ± 0.01	1.9 ± 0.4
D80 (μm)	175	166–339
Total CEC (cmol/kg)	6.02 ± 0.1	11.7 ± 3.3
Ni (mg/kg)	1,151	16
Cr (mg/kg)	704	34
Mineralogy Ca- and Mg-bearing silicate phases	Lz (29.4 wt.%), Sap (21.5 wt.%), Phl (15.1 wt.%), Fo (9.2 wt.%), Sep (2.4 wt.%), Tlc (2.2 wt.%), Aug (1.1 wt.%), Clc (0.8 wt.%)	Prg (6.5 wt.%)
Carbonates	Cal (1.9 wt.%)	Cal (16.1 wt.%)
Non-Ca, Mg-bearing phases	Mc (12.1 wt.%), Qtz (2.7 wt.%), Ab (1.7 wt.%)	Qtz (30.7 wt.%), Ab (23.4 wt.%), Mc (23.4 wt.%)

Minerals identified include Lz, lizardite; Sap, saponite; Phl, phlogopite; Fo, forsterite; Sep, sepiolite; Tlc, talc; Aug, augite; Clc, clinochlore; Cal, calcite; Mc, microcline; Qtz, quartz; Ab, albite; Prg, pargasite.

remaining oxide abundances being <1 wt.% (Table 2). Major silicate abundances included lizardite (29.4 wt.%), saponite [$M_{m+x/m}Mg_3(Al_xSi_{4-x})O_{10}(OH)_2 \cdot nH_2O$; 21.5 wt.%], and phlogopite [$KMg_3AlSi_3O_{10}(OH)_2$; 15.1 wt.%], minor abundances of forsterite (9.2 wt.%), sepiolite [$Mg_4Si_6O_{15}(OH)_2 \cdot 6H_2O$; 2.4 wt.%], talc [$Mg_3Si_4O_{10}(OH)_2$; 2.2 wt.%], and augite [$(Ca,Na)(Mg,Fe,Al,Ti)(Si,Al)_2O_6$; 1.1 wt.%], and trace abundance of clinochlore [$Mg_5Al(AlSi_3O_{10})(OH)_8$; 0.8 wt.%]. The only carbonate present was calcite (1.9 wt.%), equating to 0.25 ± 0.01% TIC (Table 1). Recalcitrant minerals in the residues that were unlikely to significantly contribute to the cation pool included microcline (12.1 wt.%), quartz (2.7 wt.%), and albite (1.7 wt.%, Table 1). Indicators of essential soil nutrient abundance, P_2O_5 and K_2O, were similar in the residues and field soils with only a slight enrichment of K_2O in the residues (Table 2). Conversely, the residues were enriched in metals of concern, Ni (1,151 mg/kg) and Cr (704 mg/kg), while these metals in the field soil were present at much lower concentrations of 16 and 34 mg/kg, respectively (Table 1).

5.2 Batch leaches with CO_2

The calcareous field soil (16.1 wt.% calcite; Table 1) mainly leached Ca (~49 g/kg) with all other elements releasing <0.5 g/kg of the initial solids content (Table 3). The Ca release substantially declined once 50% of the mixture was composed of GK residues, with the 100GK sample only releasing half (~14 g/kg) of the initial Ca content (~28 g/kg) into solution. Mg release increased with increasing GK residue proportion (~9 g/kg released from the 100GK sample; Table 3). Similarly, Si release was ~9 g/kg in the 100GK sample (<5% of the total Si available). Although field soils contained 30.7 wt.% quartz, the amount of Si leached was comparatively low (~0.5 g/kg; Table 3).

The Ni content in the leachate increased with kimberlite content (100GK: ~0.04 g Ni/kg; Table 3; Figure 3). Leachates from the field soil contained 0.7 and 0.3 μg/L of Ni and Cr, while the residue leachate contained 90 and 0.2 μg/L, respectively (Figure 3). However, Cr concentrations are within analysis noise as the blank flask of DI water yielded a Cr concentration of 0.2 μg/L (Table 3). The blank also had a Ni concentration of 3 μg/L which is lower than any flask containing >5 wt.% GK residues (Table 3).

Principal component analysis (PCA) was performed to identify the element release influenced by the kimberlite residues, which was used to distinguish kimberlite and soil weathering signals. The first two principal components (PCs) of the leachate water chemistry represented 94.7% of the total variance, with PC1 and PC2 accounting for 88% and 6.68%, respectively (Figure 4). The biplot of PCA loadings scores presents a strong negative correlation between PC1 and P, Cu, U, Al, Ti, Ca, V, and Fe, which is mainly distributed in leachates from kimberlite-poor mixtures (<50% GK; Figure 4). Positive correlation between PC1 and Mn, Co, Ni, Sr., Ba, B, Na, Si, Mg, K, and Mo indicates kimberlite residue influence and leachates from kimberlite-rich samples (≥50% GK; Figure 4). The minimal contribution from PC2 for explaining the total variance indicates a negligible influence on data interpretation.

The PCA biplot (Figure 4) represents water chemistry associated with each sample leached and identifies elements linked to the dissolution of minerals within each material. The clustering of elements indicates that the potential for target mineral dissolution influence on final leachate concentrations was significant in kimberlite-rich samples. This relationship is clear in the biplot, exhibiting a strong positive correlation and close clustering of Mg and Si within PC1.

5.3 Field experiment

The first (June 2021–November 2021), second (May 2022–December 2022), and third monitoring period (January 2023–September 2023) include data from surface CO_2 fluxes, soil porewater chemistry, and TIC with depth; overall contributing to the calculated CO_2 sequestered by kimberlite residue weathering.

5.3.1 CO_2 fluxes and soil pore gas

CO_2 flux rates were derived from instantaneous measurements and extrapolated to annual values. Fluxes were only negative (drawdown) for the K10 and K20 plots on the amendment day, −4.0 and −5.5 kg/m^2/year, and became positive (efflux) and indistinguishable from the control soil after 1 day (0.6–13.6 kg CO_2/m^2/year; Figure 5). Near negative fluxes in the control plot were only measured at the beginning of the experiment after the initial wetting of the soils when testing sampling equipment (Figure 5A). During the first monitoring period, average CO_2 fluxes were 6.5, 7.4, and 5.2 kg/m^2/year for the control, K10, and K20 plots, respectively, with peak effluxes (13.6, 18.1, and 13.8 kg/m^2/year) in August, thereafter gradually decreasing until near-net zero CO_2 emissions by November 2021 (Figure 5).

In the second and third monitoring periods, there were no negative CO_2 fluxes; however, after adding 30 kg of residues to the K10 plot in June 2022 (thereafter referred to as K10+30), fluxes decreased from 8.9 to 1.9 kg CO_2/m^2/year within 1 h (Figure 5B). In the second monitoring period, CO_2 fluxes were highest in June for the control (3.3–11.6 kg CO_2/m^2/year, avg.: 6.8 kg CO_2/m^2/year) and K10+30 (1.9–13.7 kg CO_2/m^2/year, avg.: 6.3 kg CO_2/m^2/year), and in July for the K20 (2.9–11.1 kg CO_2/m^2/year, avg.: 6.6 kg CO_2/m^2/year) plot (Figure 5). The third monitoring period showed ranges of 1.9–15.5, 1.8–12.9, and 1.4–18.1 kg CO_2/m^2/year for the control, K10+30, and K20 plots, with averages of 9.4, 7.6, and 10.2 kg CO_2/m^2/year, respectively (Figure 5).

Soil temperature at 15 cm was monitored to coincide with the soil pore gas measurements from ~20 cm and assist in the ^{13}C and ^{18}O isotopic compositions analyzed in gas samples collected at this depth. Soil temperature in the control, K10+30, and K20 yielded ranges of 0.4–32.6, 0.8–27.7, and 0.7–37.4°C over the three monitoring periods

TABLE 2 Geochemical compositions of local soils and fine processed kimberlite (FPK) given as weight percentages.

Material	Al_2O_3	CaO	Cr_2O_3	Fe_2O_3	K_2O	MgO	Mn_3O_4	Na_2O	P_2O_5	SiO_2	TiO_2	V_2O_5	$LOI_{1000°C}$
Soil	10.7	8.89	<0.01	3.97	2.14	1.44	0.12	1.87	0.27	53.3	0.53	0.01	16.8
FPK	5.04	4.03	0.16	7	2.46	27.1	0.11	0.56	0.27	42.9	0.53	0.02	9.95

TABLE 3 Initial element concentrations (g/kg) of solids and element concentrations leached from the initial material (g/kg) into solution after 2 weeks in a CO_2 incubator.

Proportion of GK residues	Concentration (g/kg)					Leached from solids (g/kg)				
	Ca	Mg	Si	Ni	Cr	Ca	Mg	Si	Ni	Cr
0GK	61.5	7.6	244	0.02	0.03	48.9	0.5	0.5	0.0005	0.0001
0.5GK	59.5	7.9	245	0.02	0.04	48.8	0.6	0.5	0.0003	0.0001
1GK	60.0	8.7	246	0.03	0.04	47.6	0.6	0.5	0.0005	0.0001
5GK	56.9	14.4	244	0.08	0.07	44.8	1.2	1.0	0.001	0.0001
10GK	57.8	22.2	242	0.1	0.1	48.4	2.0	1.7	0.002	0.0002
25GK	53.0	44.2	232	0.3	0.2	42.8	3.5	3.2	0.006	0.0002
50GK	44.9	82.0	221	0.6	0.4	30.6	6.1	6.0	0.01	0.0001
100GK	27.8	163	197	1.2	0.7	14.3	9.1	8.9	0.04	0.0001
DI Blank (mg/L)						0.02	0.003	0.2	0.003	0.0002

Labels indicate the percentage of Gahcho Kué kimberlite residues (e.g., 25GK = 25% kimberlite, 75% soil).

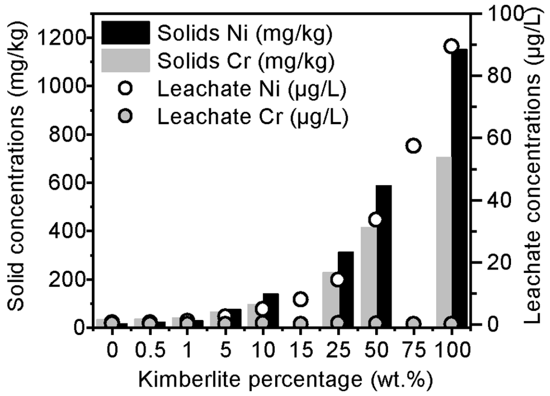

FIGURE 3
Concentrations of Ni and Cr from the flask leachates (µg/L) are represented by circles. The amount of each element in the solid soil-kimberlite mixtures (mg/kg) is represented by bars on the secondary Y-axis.

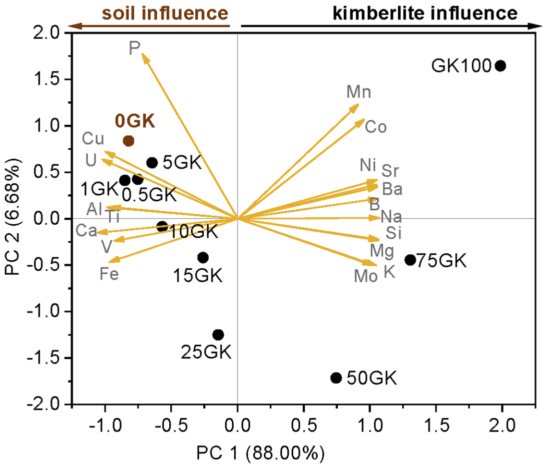

FIGURE 4
Principal component analysis (PCA) biplot showing the multivariance in 10 leached soil-kimberlite mixtures in terms of element variables. Vectors illustrate the direction and overall variable influence strength. PC1 correlates to the influence of soil (negative values) and kimberlite (positive values). Labels indicate the percentage of Gahcho Kué kimberlite residues (e.g., 25GK = 25% kimberlite, 75% soil).

with averages of 13.4, 13.2, and 13.0°C, respectively. Soil pore gas CO_2 concentrations exhibited no significant difference ($p > 0.05$) between the plots and sporadically fluctuated within a few hours yielding ranges of 0.6–1.9%, 0.4–2.1%, and 0.6–1.7% CO_2 (± 0.2%) over the first two monitoring periods.

5.3.2 Soil porewater chemistry

Porewater alkalinity differed significantly ($p < 0.05$) between shallow (15 cm) control porewaters and deeper (30 cm) K20 porewaters during the first monitoring period, and between shallow K20 porewaters and the control in the second monitoring period (Figure 6A). In the third period, porewater alkalinity at 15 cm in the K10+30 was significantly increased from all plot porewaters (Figure 6A). DIC concentrations were significantly higher ($p < 0.05$) in the K20 plot compared to the 15 cm control porewaters in the first and second monitoring periods, whereas the K10+30 plot showed a significant increase only after reamendment in 2022 (Figure 6B). Throughout the experiment, pH remained stable, with no significant differences ($p > 0.05$) between amended and control plots, fluctuating within a range of 7.2–8.2 (Figure 6C).

A distinct increase in alkalinity and DIC from 15 cm control levels (69.8 ± 7 mg C/L and 60.5 ± 12 mg C/L) occurred during the first monitoring period with values reaching averages of 80.8 ± 10 mg C/L and 72.5 ± 15 mg C/L in K10 and 92.0±16 mg C/L and 96.1 ± 13 mg C/L in K20, respectively (Figures 6A,B). The K20 plot maintained an average alkalinity of ~90 mg C/L for the next two monitoring periods but by the third period declined 67.7 mg C/L, similar to DIC values (Figures 6A,B). In the K10+30 plot, alkalinity values declined to levels similar to the 30 cm control, despite the 30 kg kimberlite addition; however, by the third monitoring period, alkalinity increased significantly in shallow porewaters, reaching the highest values recorded in the experiment (avg.: 120 ± 30 mg C/L; Figure 6A). Simultaneously, DIC in the K10+30 plot increased significantly to 93.8 ± 23 mg C/L, surpassing the K20 plot (Figure 6B). Overall, alkalinity and DIC were strongly correlated, with a maximum variance of ~20%, indicating that DIC was the primary contributor to alkalinity.

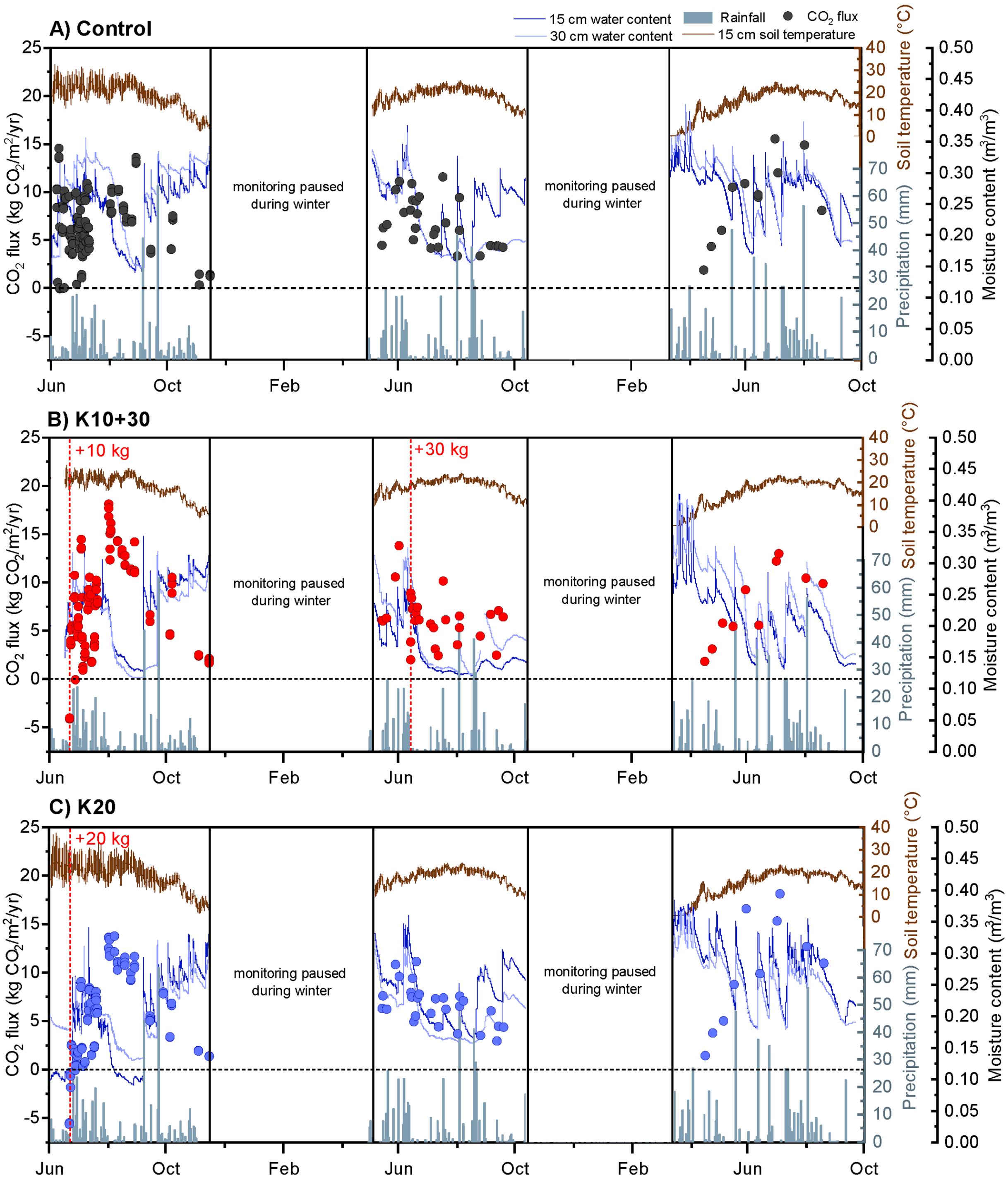

FIGURE 5
CO_2 fluxes (kg CO_2/m^2/year; solid circles) for the control **(A)**, K10+30 **(B)**, and K20 **(C)** plots at Trent University. Volumetric water contents (m^3/m^3) from moisture probes at 15 and 30 cm depths are plotted as dark blue and light blue lines, respectively, while 15 cm soil temperature (°C) is represented as a brown line. Daily precipitation (mm) is illustrated as light blue bars and is identical across all plots. Respective kimberlite dosages were added on June 23, 2021 and June 15, 2022 as denoted by the vertical red dashed lines.

All porewaters in the control were dominated by Ca (74.3–148 mg/L) with lower concentrations of Mg (1.8–3.9 mg/L), Na (1.2–7.4 mg/L), Si (1.8–6.6 mg/L), K (0.1–5.4 mg/L), Ni (0.5–1.2 μg/L), and Cr (0.03–0.3 μg/L) relative to the amended plots (n = 18–21; Figure 7). The K10 and K20 plot observed their highest Ca concentrations of 230 and 310 mg/L, respectively, in the month following the first amendment, declining to match the control for the remainder of the first monitoring period (Figure 7C). Ca concentrations peaked again in the K10+30 4 months after the addition of the 30 kg, reaching 307 mg/L before declining to control Ca levels (Figure 7C).

Kimberlite-influenced elements (e.g., Mg, Si, Na, K, and Ni) derived from PCA of the batch leach data increased above control levels after amendment; however, maximum concentrations of these

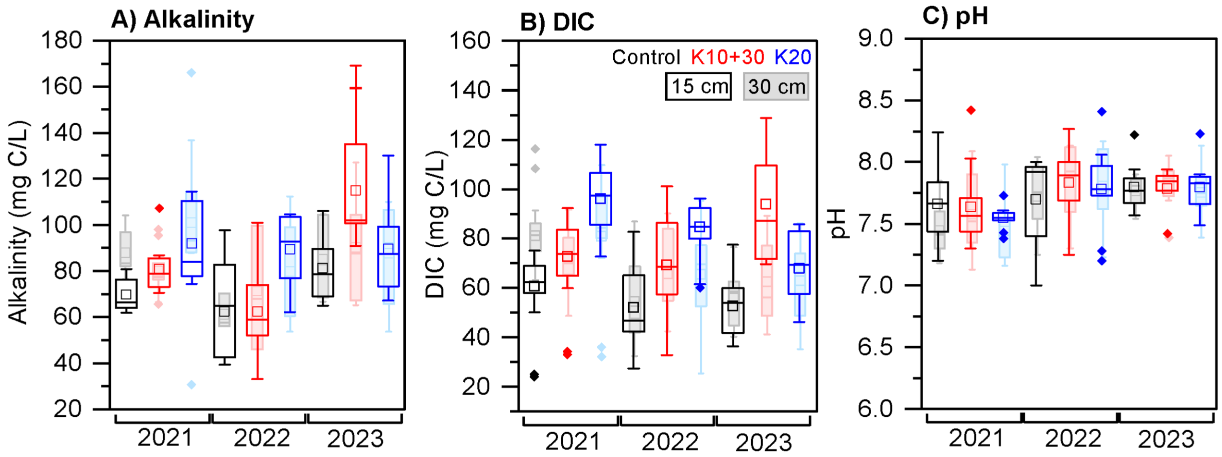

FIGURE 6
Alkalinity **(A)**, DIC **(B)**, and pH **(C)** at 15 (open box) and 30 cm (shaded) depths in the control, K10+30, and K20 plot over three monitoring periods. The rectangular box represents 25th–75th percentile range, the horizontal line inside the box is the median, the hollow square inside the box the mean, and the vertical lines outside the box are lower (5th percentile) and upper (95th percentile) whiskers. Outliers are shown as solid diamonds.

cations were observed in later monitoring periods (Figure 7). Mg ranged from 3.4–31.5 mg/L and 5.1–16.0 mg/L in the K10+30 and K20 plots, respectively, with the lowest concentrations at the end of the first monitoring period (Figure 7A). Si concentration ranges were 3.6–20.8 mg/L and 5.7–13.2 mg/L in the K10+30 and K20 plots, respectively, where both maximums occurred at the end of the third monitoring period (Figure 7B). After three monitoring periods, both Mg and Si increased by ~3 × and ~1.5 × in the K10+30 and K20 plots. Following reamendment, Na increased substantially in the K10+30 plot from initial concentrations of ~7.5 mg/L to ~130 mg/L, roughly 100 × control levels (Figure 7D). These Na concentrations declined over the next year to ~40 mg/L, whereas Na concentrations in the K20 plot had declined back to control levels (Figure 7D). Although K concentrations in the K20 plot were immediately increased and remained elevated from the control following amendment (6.0 ± 1.3 mg/L), K did not increase above control signals in the K10+30 plot until the second amendment (thereafter 9.3–22.5 mg/L; Figure 7E). Elements of concern, Ni and Cr, were highest in concentration in later monitoring periods, but remained <12 and <1 μg/L, respectively, in the amended plots (Figures 7F,G).

5.3.3 Stable C and O isotopes

The $\delta^{13}C$ and $\delta^{18}O$ values of the carbonates within the Gahcho Kué kimberlite residues averaged −11.6‰ and +19.0‰, respectively, while soil carbonate averaged −0.01‰ and +20.9‰, respectively (Figure 8). Marine carbonates (0‰) are the typical carbon isotopic signature for limestone and soils formed on limestone bedrock such as those at the field site. Negative values indicate secondary or pedogenic carbonates that result from soil weathering processes (Rabenhorst et al., 1984). As the kimberlite residues did not contain any measurable organics, only the soils were analyzed for organic isotopic signatures, averaging −27.0‰ and +9.9‰ for $\delta^{13}C$ and $\delta^{18}O$ values, respectively. These organic carbon isotopic signatures are dependent on photosynthetic pathways of plants, most commonly C3 plants (−27‰) as depicted in Figure 8.

Samples for isotopic analyses collected from the field experiments included pore CO_2 from 20 cm depths and porewater DIC from 15 cm depths. Soil pore space CO_2 yielded average $\delta^{13}C$ and $\delta^{18}O$ values of −24.3‰, −24.9‰, and −17.1‰, and +22.9‰, +28.3‰, and +25.5‰ for the control, K10+30, and K20 plots, respectively. Porewater DIC yielded $\delta^{13}C$ values of −15.5‰, −19.8‰, and −18.1‰ and $\delta^{18}O$ values of −6.5‰, −6.9‰, and −7.2‰ for the control, K10+30, and K20 plots, respectively.

5.3.4 Carbonate precipitation

No increase of TIC relative to the control was observed in either amended plot within a 25 cm soil profile in the second monitoring period, but in the third monitoring period, a ~1.5%C increase was observed in the amended plots at 15 cm below ground surface (Figure 9). The TIC of the control plot remained within a 1–2% range throughout the soil profile (Figure 9). The amended plots exhibited lower percentages of TIC at the surface and increased to control levels with depth, exceeding the control range only in the third monitoring period.

6 Discussion

6.1 Suitability of kimberlite residues for ERW

Passive carbonation of kimberlite residues has been documented at Canadian and South African mines and suggests these mine wastes could be utilized as an ERW feedstock (Wilson et al., 2011; Mervine et al., 2018; Paulo et al., 2021; Stubbs et al., 2022; Bullock et al., 2023b). The Gahcho Kué fine processed kimberlite residues, notably rich in MgO (27.1 wt.%), contain forsterite (9.2 wt.%) and lizardite (29.4 wt.%) which have been studied extensively in the context of CO_2 removal (Oelkers et al., 2008, 2018; Daval et al., 2013; Power et al., 2013b; Moosdorf et al., 2014; Farhang et al., 2017; Goll et al., 2021). These residues are also fine grained (D80 ≈ 175 μm) with high surface areas making them suitable for ERW (Lewis et al., 2021; Table 1). Similarly, South African kimberlite residues from Voorspoed and Venetia diamond mines may also be viable for ERW, having substantial abundances of Mg-silicates (e.g., lizardite and diopside), low carbonate

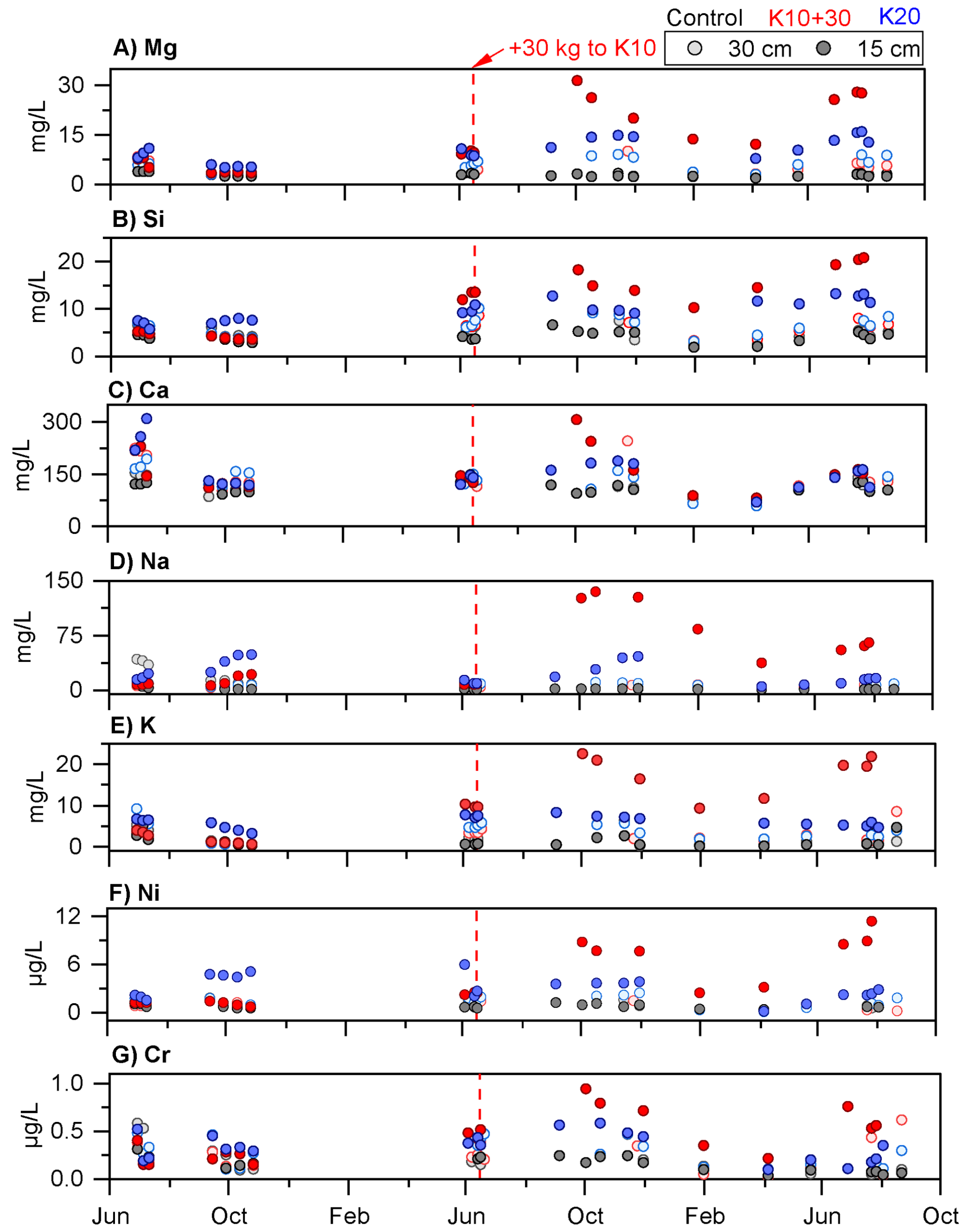

FIGURE 7
Concentrations of major cations, trace elements, and macronutrients in porewaters at 15 and 30 cm depths in the control, K10+30, and K20 plot over three monitoring periods. Larger data gaps occur when water samples were unobtainable, e.g., during winter months.

content, and minimal potential for metal and sulfur release (GK: 0.08% S; McDonald et al., 2025). Comparatively, ERW field experiments have applied basalt powders that are coarser (D80: 267–1770 μm) and with lower specific surface areas (1.0–2.7 m^2/g range) (Lewis et al., 2021; Larkin et al., 2022; Paessler et al., 2023; Beerling et al., 2024).

In comparison to global kimberlites in the Geochemistry of Rocks of the Oceans and Continents (GEOROC) database,[1] the Gahcho Kué, Venetia, and Voorspoed kimberlites have greater than average SiO_2 content (32.3 wt.%) but are below or near the CaO + MgO average (35.5 wt.%; Figure 10A). Basalt, the leading feedstock in ERW applications (Beerling et al., 2018, 2020), has a CaO + MgO average (16.5 wt.%) approximately half that of kimberlite and a higher SiO_2 average (49.2 wt.%; Figure 10A). Even kimberlites with considerable geochemical variability (e.g., Jwaneng and Orapa samples; Figure 10A), which may exhibit lower CDR potential as a result, remain enriched in CaO and MgO relative to basalt. Assuming complete carbonation of the average CaO (9.5% ± 2.2) and MgO (7.1% ± 3.1) content in basalt, 0.15 ± 0.05 t of CO_2 could be trapped as carbonate minerals per tonne of basalt, and ~0.30 t CO_2/t basalt if considering solubility trapping. Compared to the average CaO

---

[1] https://georoc.eu/

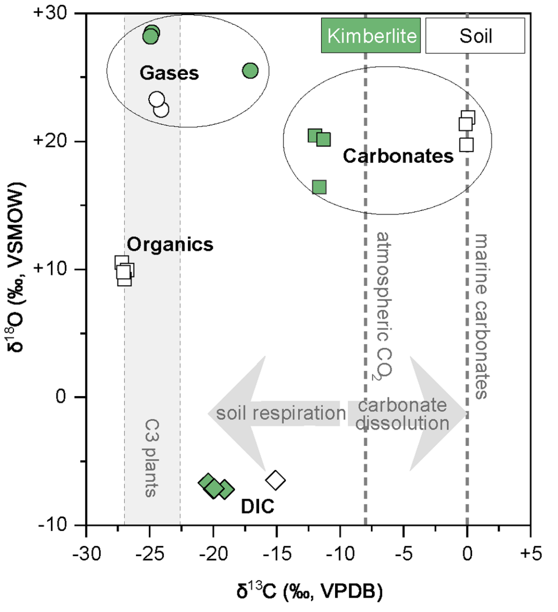

FIGURE 8
Stable carbon ($\delta^{13}C_{VPDB}$) and oxygen ($\delta^{18}O_{VSMOW}$) isotope compositions for organic and inorganic carbon in soils and kimberlite, and porewater DIC and gaseous CO_2 in the control, K10+30, and K20 plots. $\delta^{13}C$ values for marine carbonates is from Rabenhorst et al. (1984) while atmospheric CO_2, the range for soil respiration, and organics derived from C3 plants are provided by Dubois et al. (2010) and Schulte et al. (2011).

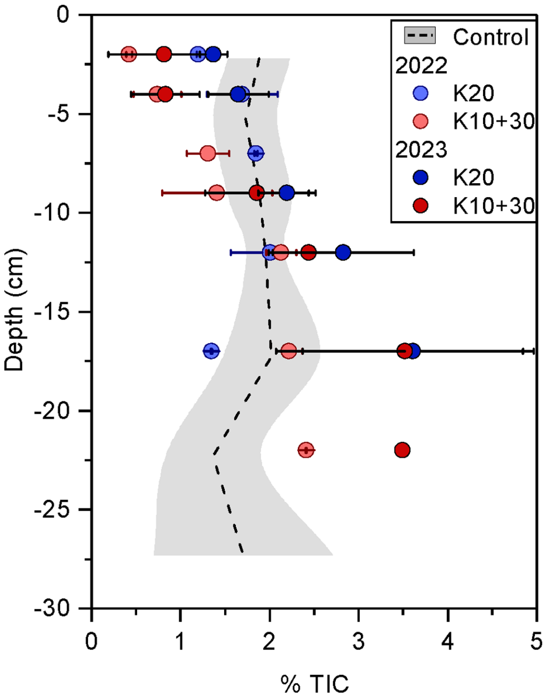

FIGURE 9
The TIC (%C) of field plot soil cores (0–25 cm) from the K10+30 and K20 plots in 2022 (n = 6) and 2023 (n = 6), approximately 1 year apart. The control range for TIC is averaged over the second and third monitoring periods (n = 12).

(10.7% ± 6.4) and MgO (24.8% ± 7.3) content in kimberlite, complete reaction would sequester 0.35 ± 0.13 t CO_2/t kimberlite as carbonate or ~0.70 t CO_2/t kimberlite as dissolved inorganic carbon.

Kimberlite and basalt both contain several relatively fast-weathering silicate minerals that are of interest for CO_2 removal. For example, laboratory dissolution rates of forsterite ($10^{-10.6}$ mol/m^2/s at pH 7) and pyroxene minerals (10^{-12} to $10^{-11.1}$ mol/m^2/s) are some of the fastest rates among the minerals present in each rock type (Palandri and Kharaka, 2004). Primary differences in mineralogy include higher abundances of plagioclase feldspars ($10^{-12.6}$ to $10^{-10.9}$ mol/m^2/s) and varying abundances of amorphous glass ($10^{-11.9}$ mol/m^2/s) in basalt (Lewis et al., 2021), and considerable quantities of serpentine minerals (e.g., lizardite: $10^{-12.4}$ mol/m^2/s) in kimberlite (Mervine et al., 2018; Kjarsgaard et al., 2022). Serpentine minerals contribute the most to the CDR capacity of kimberlites owing to their high potential for Mg release, large surface areas to facilitate reactions with CO_2, and high abundance (Power et al., 2013a, 2013b). One mineral group, common in basalt and kimberlite, that has gained increasing attention for CDR potential are smectites ($10^{-12.8}$ mol/m^2/s; Palandri and Kharaka, 2004; Zeyen et al., 2022). In kimberlites, the reactivity of the smectite mineral saponite contributes to high specific surface areas (13.8–48.0 m^2/g; Mervine et al., 2018) and provides a significant source for cation exchange, releasing labile interlayer Mg and Ca ions rather than from dissolution (Zeyen et al., 2022).

Basalt is likely a preferred feedstock in agricultural ERW applications based on the low Ni (avg. = 125 mg/kg) and Cr (avg. = 258 mg/kg) concentrations according to the GEOROC database (Figure 10B) and low metal leaching potential (e.g., 0.05% total Ni released; te Pas et al., 2023). However, non-agricultural application sites may allow higher thresholds for metal concentrations, in which the GEOROC average Ni (1,036 mg/kg) and Cr (1,286 mg/kg) content in kimberlite may be acceptable. Kimberlites typically contain higher levels of beneficial nutrients (e.g., P and K GEOROC averages of 2,332 and 9,814 mg/kg) compared to basalts (1,762 and 9,244 mg/kg, respectively), suggesting suitability for mine closure purposes (Figure 10C). As kimberlite residues are enriched in MgO improving their CDR capacity, possess a greater abundance of fast weathering Mg-silicates, and exhibit potential for co-benefits, kimberlite is likely a suitable rock type for certain ERW applications.

6.2 Leaches: reactivity assessment and predictors of water chemistry

The leaching tests were used to assess the reactivity of kimberlite residues in terms of easily released cations and their respective mineral origins. These tests are similar to those conducted by Paulo et al. (2021) and McDonald (2023) to quantify easily extractable cations from mine tailings and ERW feedstocks. Within 2 weeks, half of the Ca content (2.8 wt.%) in the 100GK flasks was released (14.3 g/kg; Table 3), primarily from calcite (1.9 wt.%) dissolution, evident in the increase in pH value from 5.5 to ~6.5. Although Mg (16.3 wt.%) and Si (19.7 wt.%) concentrations were high, release of these elements was relatively low compared to Ca (9.2 and 8.9 g/kg; Table 3), indicating slower dissolution of Mg-silicate phases (Figure 4; Pokrovsky and Schott, 2000; Brantley and Olsen, 2014; Heřmanská et al., 2023). Although other Mg-bearing phases present at lower abundances (e.g., sepiolite, talc, augite, and clinochlore) are not likely to significantly

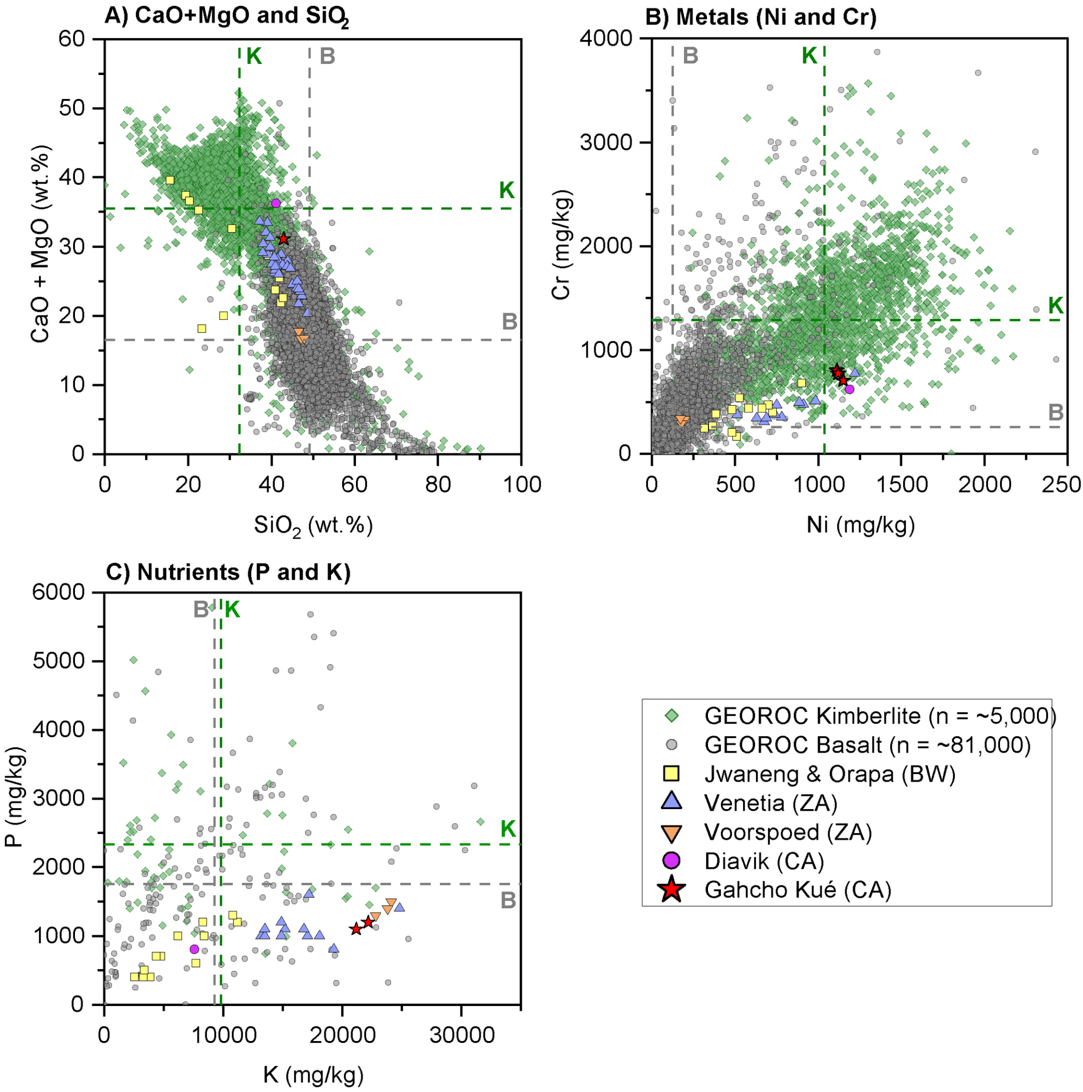

FIGURE 10
Concentrations of CaO + MgO and SiO_2 (wt.%; **A**), Ni and Cr (mg/kg; **B**), and P and K (mg/kg; **C**) in the whole rock geochemistry of kimberlite (K) and basalt (B) samples sourced from the GEOROC database (https://georoc.eu/). Additional kimberlites from Botswana, South Africa, and Canada are plotted for comparison. Dashed lines indicate the average parameters for kimberlite (green) and basalt (gray) samples in the GEOROC database.

contribute to the cation pool, cation exchange with saponite (21.5 wt.%) could appreciably enhance cation release (Zeyen et al., 2022). The presence of recalcitrant silicate minerals (e.g., quartz 30.7 wt.%; Table 1) in the soil explains the lower Si release (0.4 g/kg) compared to the leaches containing the kimberlite residues (Table 3). This finding indicates that Si signals in mixed material flasks originate primarily from kimberlite silicate dissolution.

The experimental field plot amendment was equivalent to the 5GK (K20) and 10GK (K10+30) mixture leaches by mass if considering a 30 cm soil profile with an average bulk density of 1.2 g/cm³. In a 15 cm profile the K20 and K10+30 plots contained 10 wt.% (10GK) and 25 wt.% (25GK) kimberlite, respectively. Considering kimberlite-influenced elements only became strongly correlated with kimberlite content in mixtures of at least 50 wt.% kimberlite—a dosage of 90 kg/m² with a mixing depth of 15 cm—cations signals were expected to be dominated by soil mineral weathering (Figure 4). Additional or higher amendment applications would likely improve amendment weathering detection by composing a greater proportion of the soil system, although this risks porewater saturation of key minerals reducing CDR efficiency.

The maximum CDR potential (CDR_{pot} in tonnes of CO_2 per tonne of material) achieved by the GK residues was estimated using the modified Steinour equation (Steinour, 1959) used by Clarkson et al. (2024) (Equation 1).

$$CDR_{pot} = \frac{M_{CO2}}{100\%} \times \left[\frac{MgO\%}{M_{MgO}} + \frac{CaO\%}{M_{CaO}} + \frac{K_2O\%}{M_{K2O}} + \frac{Na_2O\%}{M_{Na2O}} \right] \times \omega \quad (1)$$

Where M is the molar mass of the subscripted compound and ω ranges from 1.5 to 1.7 and represents the additional drawdown per cation flux into the ocean. Based on the kimberlite oxide contents (wt.% of MgO, CaO, K_2O, and Na_2O), the Gahcho Kué residues could remove 500–567 kg CO_2/t. McDonald (2023) conducted reactivity tests using 100% CO_2 and estimated the CO_2 sequestration potential of Gahcho Kué residues at 11.9 kg CO_2/t based on easily extractable cations from non-carbonate sources. For comparison, Paulo et al. (2021) and McDonald (2023) estimated the CO_2 sequestration potential of Venetia residues to be ~1–4 × lower than that reported by McDonald (2023) for the Gahcho Kué residues.

While these leaches facilitated mineral dissolution beyond what is expected in the field, they are useful for assessing reactivity, evaluating potential metal release, and understanding cation release. Specifically, Si release is mainly attributed to kimberlite silicate dissolution, and Ca release attributed to carbonate dissolution in the soil and kimberlite. These insights were used to differentiate between soil mineral and kimberlite mineral dissolution in the field experiment.

6.3 Quantifying CO_2 removal

Accurately quantifying carbon removed by ERW requires a comprehensive understanding of the numerous geochemical processes and CDR pathways and how mineral weathering is intricately linked to fluid interactions, underscoring the importance of monitoring soil waters. Carbon coulometry is a precise method for measuring DIC and TIC to quantify solubility and mineral trapping, respectively (Figure 11). Conversely, assessing CO_2 fluxes presents a challenge due to the overwhelming CO_2 release from soil respiration that masks relatively minute CO_2 drawdown (Figures 4, 11). Thus, the CO_2 fluxes measured in this study were not useful in the quantification of CO_2 in these organic environments and instead quantification relied on results from carbon coulometry.

Cation mass balances and carbon phase measurements are commonly used in ERW studies such as in column or pot experiments (ten Berge et al., 2012; Renforth et al., 2015; Amann et al., 2020; Pogge von Strandmann et al., 2022; te Pas et al., 2023) and in field trials (McDermott et al., 2019, 2024; Haque et al., 2020b; Larkin et al., 2022; Maxbauer and Yambing, 2022; Vink et al., 2022; Guo et al., 2023; Kantola et al., 2023; Paessler et al., 2023; Beerling et al., 2024). However, the small CDR signals can be obscured by the substantial background noise in natural soils (Calabrese et al., 2022). To address this limitation, stoichiometric mineral reactions with CO_2 have been used to estimate carbon capture based on the measured weathering products (e.g., Mg; Dietzen and Rosing, 2023; Iff et al., 2024). As element proxies assume all cation loss results from leached cations reacting with carbonic acid to generate bicarbonate, this approach does not consider the fate of the numerous carbon phases and only offers an upper estimate of CDR (Clarkson et al., 2024). However,

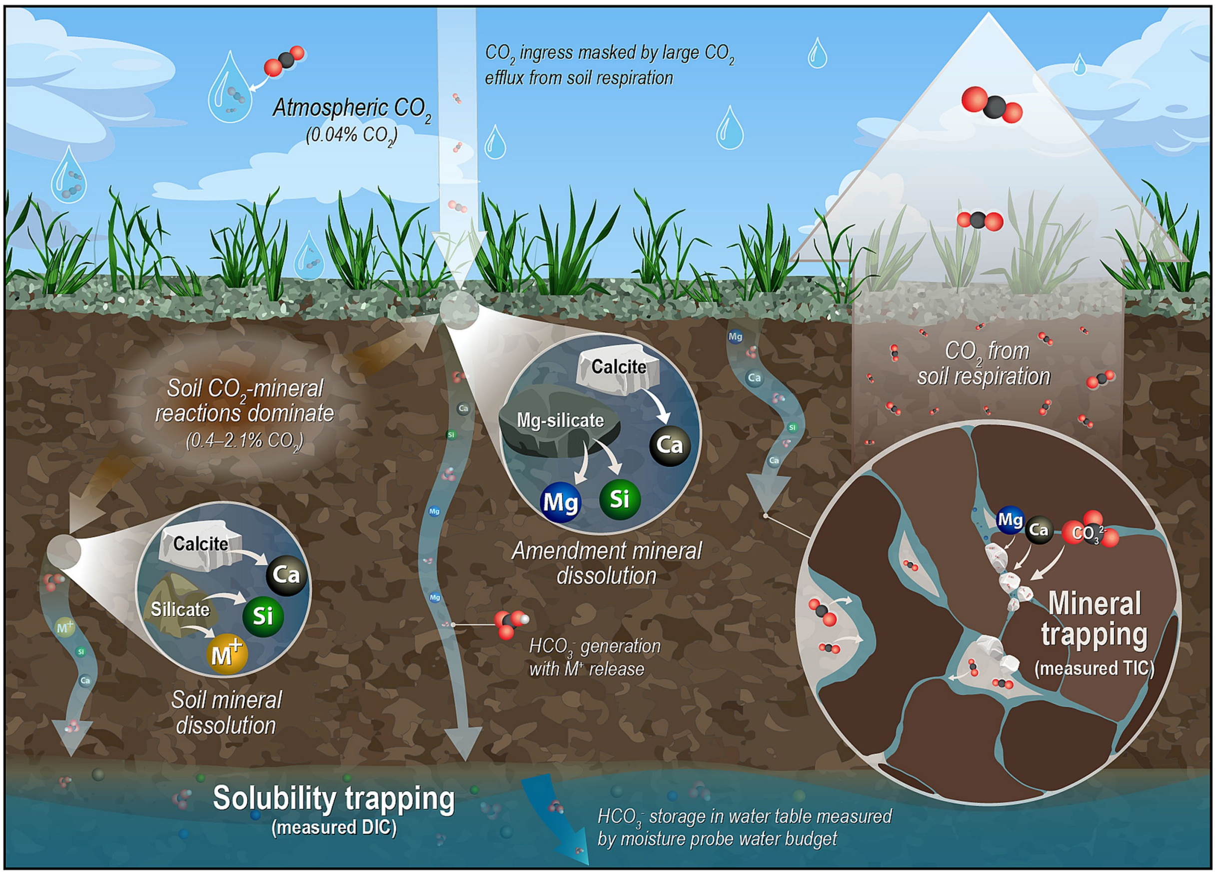

FIGURE 11
Conceptual diagram illustrating geochemical processes facilitating solubility trapping and CO_2 mineralization. Slightly acidic rainfall facilitates soil and amendment mineral weathering, releasing cations into solution generating bicarbonate anions, which can be measured as DIC, or precipitate as carbonate minerals, which can be measured as TIC. CO_2 emissions from soil respiration are depicted as large effluxes that mask the minimal ingress of CO_2 due to mineral weathering.

monitoring element release relative to the amount of feedstock applied can provide insight into which minerals are likely contributing to CDR.

Identifying the prominent weathering minerals within the amendment and their respective molar ratios when removing CO_2 ensures accurate partitioning of total CDR rates. In this study, forsterite and lizardite were the dominant silicates in the kimberlite amendment, leaching Si into porewaters. Based on Equations 2, 3, forsterite and lizardite weathering generate four and three moles of HCO_3^- for every mole of Si, respectively. Additionally, for every mole of Ca released from calcite weathering (Equation 4), two moles of HCO_3^- are generated; however, this ratio includes the CO_2 within the calcite structure, necessitating halving of this ratio to only account for newly removed CO_2.

$$Forsterite: Mg_2SiO_4 + 4CO_2 + 2H_2O \rightarrow 2Mg^{2+} + 4HCO_3^- + H_4SiO_4 \quad (2)$$

$$Lizardite: Mg_3Si_2O_5(OH)_4 + 6CO_2 + 5H_2O \rightarrow 3Mg^{2+} + 6HCO_3^- + 2H_4SiO_4 \quad (3)$$

$$Calcite: CaCO_3 + CO_2 + H_2O \rightarrow Ca^{2+} + 2HCO_3^- \quad (4)$$

Monitoring soil porewaters determines bicarbonate and cation export presumably to the water table (solubility trapping) and soil sampling with depth evaluates carbonate formation throughout the soil profile (mineral trapping). Regardless of the CDR pathway, a better understanding of site-specific hydrology and porewater chemistry is necessary.

6.3.1 Hydrology and water balance

Timing of porewater sampling should best reflect the local water budget, e.g., after precipitation and during drying periods. However, continuous measurements of soil moisture are necessary for monitoring upper profile recharge and lower profile percolation to determine a site-specific water balance. Soil moisture levels are quantified volumetrically, expressed as cubic meters of water per cubic meter of soil. In this methodology, shallow (15 cm) moisture probes were assumed to detect all rainfall and calibrated so that any increase in moisture corresponded directly to the amount of rainfall during the observed period. This soil-specific calibration established a direct relationship between moisture values and soil water content. For instance, consider that 1 mm of rainfall equates to 1 L over a 1 m^2 plot. Using this conversion, ~50 moisture increases measured in the control plot were selected to correlate to rainfall events, resulting in a linear relationship, as described by Equation 5.

$$\Theta = 0.0031V + 0.0036 \quad (5)$$

where Θ is the recorded volumetric water content (m^3/m^3) and V is the volume of water (L) in the system correlated with that moisture reading. Some evaporation, residual moisture, and recharge in the upper profile were expected; hence, the deeper (30 cm) moisture probes recorded dampened responses of soil moisture from rainfall inputs. Equation 5 was used to convert the 30 cm moisture to a volume of soil water in the control and amended plots.

Recent protocols for calculating CO_2 removal stipulate that ERW products transported to a depth of at least 30 cm are regarded as removed carbon (Sutherland et al., 2023—Isometric). Therefore, percolation values in this study comprised of the volume of water passing the 30 cm probe (Supplementary Table S3). These values assumed negligible lateral flow due to the site possessing no significant slope, and negligible evaporation at depth. Percolation values (V_P) were calculated by determining the difference in average soil water content over 2 h intervals and summing them to derive monthly percolation values (Equation 6).

$$V_P = \sum_{i=1}^{N_{mo}} \Delta\Theta_i \quad (6)$$

where mo represents each month from 1 to 12, N_{mo} is the total number of 2 h intervals in month mo, and $\Delta\Theta_i$ is the change in moisture for each 2 h interval in month mo. Typically, ~60% of total rainfall recorded during each monitoring period percolated past 30 cm. To estimate annual CO_2 removal via DIC and quantify carbonate and silicate weathering through Ca and Si loadings, a percolation factor was introduced. However, because CDR rates are highly sensitive to percolation values, inaccuracies in soil drainage estimates can introduce significant error.

To assess uncertainty in percolation values, error bars in Figure 12 represent two boundary estimates: an upper maximum assuming that all rainfall percolated past 30 cm (~800 L/yr) and a lower minimum assuming a conservative 25% of total rainfall contributed to soil water recharge (~200 L/yr). The lower boundary closely aligns with hydrogeological studies from Southern Ontario (Parkin et al., 1999; Brown et al., 2013), which monitored precipitation percolating past the rooting zone in agricultural loam and Brunisols. Further, Parkin et al. (1999) highlighted substantial year-to-year variability in deep percolation volumes, emphasizing the importance of continuous moisture monitoring when quantifying solubility trapping rates. Water infiltration (i.e., water interacting with the feedstock) and soil drainage (i.e., percolation and storage of generated alkalinity) are primary influences on mineral dissolution efficiency and CDR rates and must be understood for each field trial.

6.3.2 Quantifying CO_2 removal by solubility trapping

Monthly quantities of total CO_2 removed were calculated using DIC, a direct measurement of carbon in waters. The DIC measured in the monitored months was multiplied by the ratio of yearly precipitation to the precipitation during the monitoring period to extrapolate the data to 1 year and address data gaps when sampling was limited (e.g., winter). These rates were compared to those calculated using alkalinity expressed as HCO_3^-. The concentrations used in these calculations are water leachates from the 15 cm sampler, as mineral weathering detections in the lower profile for all parameters were less apparent. CDR rates using DIC and alkalinity were calculated using Equations 7, 8, respectively.

$$CDR\left(g\ CO_2/m^2/yr\right) = \sum_{mo}\left[\left([DIC]\times V_P\right)\times\frac{1\,g}{1000\,mg}\times\frac{M_{CO_2}}{M_C}\right]\times\left(\frac{P_{year}}{P_{period}}\right) \quad (7)$$

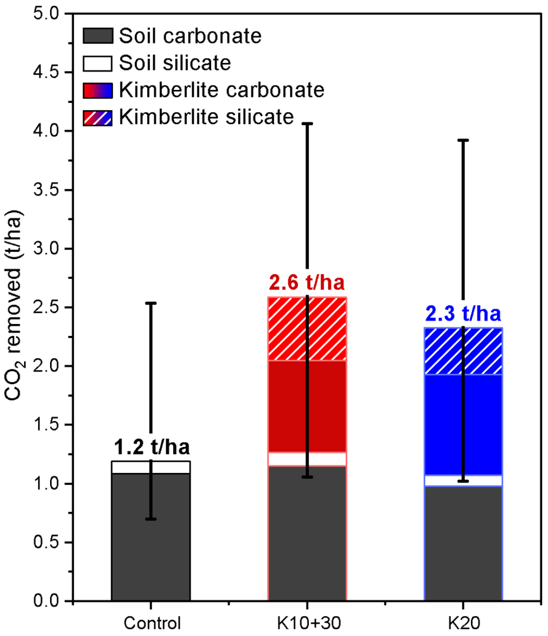

FIGURE 12
Cumulative CO_2 removal (t CO_2/ha) over 3 year calculated via DIC and divided into carbonate and silicate weathering of the soil and kimberlite residues in the control, K10+30, and K20 plots. Error bars represent the uncertainty in percolation volume estimates, with the upper bound assuming 100% of rainfall percolated past 30 cm, and the lower bound indicating only 25% of rainfall percolated past 30 cm.

$$CDR\left(g\,CO_2/m^2/yr\right)= \sum_{mo}\left[\left(\left[Alk\right]\times V_P\right)\times\frac{1\,g}{1000\,mg}\times\frac{M_{CO_2}}{M_{HCO_3^-}}\right]\times\left(\frac{P_{year}}{P_{period}}\right) \quad (8)$$

where $[DIC]$ and $[Alk]$ are the average concentrations (mg C/L) for the respective parameter over each month, V_P is the total percolation volume (L) for the respective month, and M_{CO2}, M_C, and M_{HCO3}- are the molar masses of each form of carbon. The sequestered CO_2 for each month was summed and extrapolated to 1 year by multiplying by annual precipitation (P_{year}) and dividing by the precipitation amount during the monitoring period (P_{period}; Supplementary Table S3).

The K10+30 and K20 plots exhibited comparable CDR rates, achieving 2.6 and 2.3 t CO_2/ha over 3 years, respectively, whereas the local soil had a CO_2 consumption rate of 0.4 t CO_2/ha/year (Figure 12). Accounting for percolation volume uncertainty, solubility trapping rates over 3 years potentially fall in the ranges of 0.7–2.6 t CO_2/ha for the control, 1.1–4.1 t CO_2/ha for K10+30, and 1.0–3.9 t CO_2/ha for K20 (Figure 12). Contributed by solely kimberlite weathering, the amendment in the K10+30 and K20 plot removed 1.4 (0.3–1.4) and 1.3 (0.4–1.5) t CO_2/ha over 3 years, a fraction of the CDR potential calculated using the Steinour equation (Equation 1; K10+30: 50–227 t CO_2/ha, K20: 100–113 t CO_2/ha).

Carbonate weathering must be considered for calcareous soils and carbonate-bearing amendments. Importantly, CDR rates must exclude removed carbon originating from carbonates (Equation 4). Therefore, CO_2 removal contributed by calcite dissolution was conservatively halved and corrected in the overall CDR derived from DIC measurements (McDermott et al., 2024). The total CDR rate can be conceptualized as the sum of silicate and carbonate weathering components from the soil and the amendment (Figure 11; Equation 9):

$$CDR_{total}=\left(CDR_{silicate}+CDR_{carbonate}\right)_{Soil} +\left(CDR_{silicate}+CDR_{carbonate}\right)_{Amendment} \quad (9)$$

where CDR_{total} is the total amount of CO_2 stored via solubility trapping calculated by DIC content in drainage waters, including CO_2 removed from the atmosphere or soil pore gas and carbonate weathering (Equation 7). The proportions of CO_2 removal contributed by carbonate ($CDR_{carbonate}$) and silicate ($CDR_{silicate}$) weathering of the soil and kimberlite minerals were determined by comparing the Ca and Si concentrations, respectively. The additional CO_2 removal by kimberlite carbonate and silicate weathering was based on the increase in Ca and Si concentrations in porewaters compared to the control plot. The mineral weathering removal rates using cation release were calculated using Equations 10, 11, yielding calcite weathering contributions amounting to ~72–78% and silicate weathering contributing ~22–28% of the CDR_{total} in the amended plots.

Carbonate weathering contribution:

$$CDR_{carbonate}\left(g\,CO_2/m^2/yr\right)= \sum_{Month}\left[\left(\left[Ca\right]\times V_P\right)\times\frac{1\,g}{1000\,mg}\times{}^{1}\!/_{2}\,\frac{M_{CO_2}}{M_{Ca}}\right]\times\left(\frac{P_{year}}{P_{period}}\right) \quad (10)$$

Silicate weathering contribution:

$$CDR_{silicate}\left(g\,CO_2/m^2/yr\right)= \sum_{Month}\left[\left(\left[Si\right]\times V_P\right)\times\frac{1\,g}{1000\,mg}\times n\,\frac{M_{CO_2}}{M_{Si}}\right]\times\left(\frac{P_{year}}{P_{period}}\right) \quad (11)$$

where $[Ca]$ and $[Si]$ are the average concentrations (mg/L) for the respective cation for that month, n is substituted for the number of moles reacting to form HCO_3^- if assuming 100% lizardite contribution ($n = 3$; Equation 3) or 100% forsterite contribution ($n = 4$; Equation 2), and M_{Ca} and M_{Si} are the molar masses of the respective cation. Impacts from other strong acid weathering agents were expected to be negligible as sulfide minerals were not present (GK: 0.08% S) nor was there any recent use of nitrogen fertilizers at the study site. Concentrations of NO_3^- and SO_4^{2-} were low throughout the experiment (Supplementary Figure S1), providing a negligible shift in the cross plot of HCO_3^- and major cations (remaining below or on a 1:1 line until corrected for Cl concentrations; Supplementary Figure S3). Furthermore, non-carbonic acid neutralization can be approximated based on soil pH and pCO_2, where a pCO_2 value at least 10 times atmospheric suggests that if the pH is above 5.99, which these porewaters are (Figure 6C), stronger acid weathering is negligible (Dietzen and Rosing, 2023).

Carbonate dissolution with the aforementioned strong acids is a source of CO_2 emissions and most commonly occurs in agricultural liming practices accompanied by extensive fertilizer use (West and

McBride, 2005). As a result, the dominating opinion on carbonate weathering is that it is a direct source of CO_2 and negates much of the CO_2 removed contributed by silicate weathering. Many rock powders applied for ERW contain minor abundances of carbonates (e.g., see Lewis et al., 2021) that contribute to cation and DIC release, particularly given that carbonate dissolution rates are orders of magnitude faster than silicates. If soils are acidic due to strong acids (e.g., HNO_3), carbonate weathering will release CO_2, or if downstream waters are supersaturated with respect to carbonate minerals, re-precipitation will reverse CO_2 removal (Power et al., 2025). However, where weathering via carbonic acid dominates (Equation 4) and carbonate precipitation in downstream waters does not occur (Knapp and Tipper, 2022), the fast-reacting carbonates may contribute meaningful bicarbonate export (Oh and Raymond, 2006). A recent example of rapid calcium release and bicarbonate generation persisted in a field trial that applied carbonate-rich concrete (71.1 wt.% calcite) to a fertilizer-free farm plot, highlighting the value of quick-weathering industrial wastes characterized by accessory carbonates for solubility trapping (McDermott et al., 2024). With pressing need for annual Gt removal of CO_2, the fast dissolution rates of carbonate minerals may be required for rapid CDR to mitigate climate change (Liu et al., 2011; Knapp and Tipper, 2022).

Our methodology draws from the widely adopted practice of monitoring DIC and alkalinity for quantifying carbon removal via solubility trapping in ERW experiments (Amann et al., 2020; Kelland et al., 2020; Taylor et al., 2021; Amann and Hartmann, 2022; Larkin et al., 2022; Vienne et al., 2022; Guo et al., 2023; Knapp et al., 2023; te Pas et al., 2023). A hectare-scale field trial in Sabah, Malaysia using a single 50 t/ha dose of andesitic basalt achieved a maximum CO_2 removal of 1.0 t CO_2/ha over 3 years (Larkin et al., 2022), measured via alkalinity in catchment stream waters. In contrast, this study used moisture probes to derive a water budget for calculating inorganic carbon loadings. In the United States Corn Belt, metabasalt application for 4 years at 50 t/ha/year yielded higher removal rates (6.7–14.3 t CO_2/ha over 4 years) using an element mass balance approach using Ti immobility as a proxy for basalt weathering (Beerling et al., 2024). The Carbon Drawdown Initiative applied the same method, recognizing it as an indicator of the upper limit for CDR rates. They reported 4–8 t CO_2 removed over 8 months, with improved CDR efficiency in plots amended with a 100 t/ha dosage compared to a 400 t/ha dose (Paessler et al., 2023). The high dosages used in this study ensured solubility trapping detection and allowed for accurate partitioning into mineral weathering contributions derived from cation loadings. The easily detectable concentrations of kimberlite-influenced elements (e.g., Mg, Si, Na, K, and Ni) observed shortly after amendment were likely a result of initially rapid leaching of labile cations (Paulo et al., 2021; Lu et al., 2022). However, despite distinct kimberlite weathering signals from soil weathering, the delay in further element concentration increases suggests a possible lag in cation transport (Figure 4; Figure 7), with expected lag times potentially ranging from years to decades depending on the cation exchange capacities of the background soils (Kanzaki et al., 2024).

6.3.3 Quantifying CO_2 removal by mineral trapping

Kimberlite weathering and release of Ca and Mg could potentially facilitate precipitation of carbonate minerals (e.g., calcite), storing CO_2 by mineral trapping in addition to the previously described solubility trapping quantified using DIC. Calcite remained supersaturated in porewaters throughout the experiment with greater saturation for the amended plots (Supplementary Table S2). Furthermore, dolomite supersaturation surpassed calcite in the amended porewaters in all monitoring periods (Supplementary Table S2), reflecting Mg release from the kimberlite residues. CO_2 removed via mineral trapping was calculated based on changes in soil TIC content using Equation 12.

$$Mineral\ trapping\left(g\ CO_2/m^2\right)=\left(\frac{\Delta TIC}{100}\times\frac{m_{soil}}{m^2}\right)\times\frac{M_{CO_2}}{M_C} \qquad (12)$$

where ΔTIC is the change of TIC (%) between the segmented initial and final soil cores, and m_{soil} is the estimated mass of soil in a square meter with a thickness of 10 cm (0–10 cm) and 15 cm (10–25 cm) based on a bulk density of 1.2 g/cm^3 (Supplementary Table S1). Initial TIC content was derived from averaging values measured in 2–5 cm increments throughout ~25 cm cores collected from the control plot in 2022 and 2023 ($n = 12$). The addition of kimberlite decreased the average TIC in the upper profile given that the amendment had less calcite compared to the soils which possessed ~45 kg (1.8%C ± 0.4) in a square meter profile to a depth of 25 cm (Figure 9). Still, there was approximately 0.8 and 0.4 kg of calcite added to the K10+30 and K20 plots. The CO_2 removed via mineral trapping and solubility trapping achieved by kimberlite weathering is summarized in Table 4.

The observed TIC increase (K10+30: 32.5 kg ± 50, K20: 35.0 kg ± 42 of carbonate) was a mixture of the existing calcite in the soil, re-precipitated pedogenic carbonates, and calcite in the kimberlite. Differentiating these sources pose a challenge in accurately accounting for mineral trapped CO_2. These mineral trapping rates in addition to the solubility trapping rates would increase the total amount of CO_2 sequestered via kimberlite weathering substantially; however, the large uncertainty in TIC measurements due to soil heterogeneity results in uncertainty in the overall CDR rate (Table 4). Furthermore, the high and variable TIC content of the calcareous soils makes mineral trapping quantification unreliable.

Relatively high removal rates via mineral trapping have been demonstrated previously in ERW experiments (Manning et al., 2013; Haque et al., 2019; Vienne et al., 2022). Basalt, which contained no carbonates, applied to a mixture of dolerite and local soil (~0.1 wt.% $CaCO_3$) produced an annual mineral trapping rate of ~18 t CO_2/ha (Manning et al., 2013). Vienne et al. (2022) report a TIC increase of 12.4 t CO_2/ha after 99 d of basalt weathering, but with a high standard deviation that exceeds this rate (± 24.7 t CO_2/ha). Most basalts are characterized by trace amounts of calcite (typically <1 wt.%), which when weathered have demonstrated the potential to reduce CDR rates by 3% (Tawau basalt: 0.6 wt.% $CaCO_3$) to 30% (Cragmill basalt: 1.2 wt.% $CaCO_3$; Lewis et al., 2021). Assuming the entirety of calcite

TABLE 4 CDR (t CO_2/ha) of kimberlite weathering based on changes in TIC (mineral trapping) and DIC (solubility trapping) over 3 years.

Field plot	Mineral trapping (t CO_2/ha)	Solubility trapping (t CO_2/ha)	Total sequestration (t CO_2/ha)
K10+30	61 ± 66	1.4	62.4 ± 66
K20	89 ± 44	1.3	90.3 ± 44

content in the kimberlite amendment weathered out over 3 years and re-precipitated (K10+30: +0.04%C, K20: +0.02%C), removing the same amount of CO_2 as initially released during weathering (K10+30: ~4 t CO_2/ha, K20: ~2 t CO_2/ha), the maximum CDR relative to mineral trapping equates to a fraction of what was measured (Table 4).

6.4 CO_2 sources

As in other ERW applications, potential sources of carbon sequestered in the field plots included atmospheric CO_2 (0.04%) and soil pore gas CO_2 (0.4–1.9%) derived from microbial respiration (Figure 11). It is worth noting that soil pore CO_2 concentrations were 10 to nearly 50 times greater than atmospheric CO_2 concentrations. While CO_2 fluxes were negative or less positive immediately following kimberlite amendment due to the initial reactivity of the material (Figures 5B,C), soil CO_2 fluxes became indistinguishable between the control and amended plots (Figure 5). Maximum CO_2 removal capacities (Equation 1) of the kimberlite residues are within the expected variability of soil CO_2 respiration rates. Therefore, soil CO_2 effluxes would mask any drawdown even if complete reaction occurred within 1 year. This finding highlights the high effluxes of soils and the inability of this method to reliably measure CO_2 removal by ERW. ERW is often described and depicted removing CO_2 from the atmosphere; however, soil CO_2 is likely the dominant source given its much greater concentration. Nevertheless, this biogenic carbon is mostly derived from the atmosphere, fixed through photosynthesis (Wood et al., 2023; Figure 11).

Stable carbon isotope data provides further evidence that DIC in soil porewaters originates from organic sources (Figure 8). The ^{13}C compositions of the soil organic carbon (avg. $\delta^{13}C = -27.0‰$) are consistent with organics derived from C3 plants (−23‰ to −27‰; Schulte et al., 2011). While microbial respiration of the organic matter does not result in isotopic fractionation, soil pore gas (avg. $\delta^{13}C = -24.2‰$) was enriched in ^{13}C by +2.8‰, suggesting some mixing of atmospheric CO_2 ($\delta^{13}C_{atm}$: −7.7‰; Schulte et al., 2011) either prior to or during sampling (Figure 8). The fractionation between gaseous CO_2 and dissolved bicarbonate at circumneutral pH is +9.0‰ at 15°C, the approximate pH of the soils (Mook et al., 1974). Given the ^{13}C composition of the pore CO_2, $\delta^{13}C_{DIC}$ values of approximately −18.0‰ would be expected. Porewater $\delta^{13}C_{DIC}$ values averaged −15.5‰, −19.8‰, and −18.1‰ for the control, K10+30, and K20 plots, respectively, consistent with the organic respiration range defined by Dubois et al. (2010). Thus, ERW primarily suppresses soil respiration rather than directly removing atmospheric CO_2. While the result is similar, this distinction and identification of the CO_2 source are important in the context of accurate CDR quantification.

Soil inorganic carbon $\delta^{13}C$ values are near zero or slightly positive, reflecting typical values for marine carbonates (e.g., limestone; Figure 8; Rabenhorst et al., 1984). Inorganic carbon isotopic signatures of bulk Gahcho Kué kimberlite residues are within the ranges reported by Giuliani et al. (2014) for $\delta^{13}C$ (−11.9‰ to +0.2‰) and $\delta^{18}O$ (+1.2‰ to +26.6‰), reflecting a global composition of kimberlites. While the kimberlite residues may shift bulk ^{13}C and ^{18}O compositions of amended soil given the high dosages, carbonate precipitation incorporating biogenic CO_2 in soil is unlikely to alter these isotope values as the soil TIC was exceedingly high.

6.5 Metal and nutrient release

While batch leaches showed minimal metal release from the kimberlite residues, prolonged weathering of ultramafic feedstocks could lead to the accumulation of adverse elements (e.g., Ni and Cr; Dupla et al., 2023), posing risks to the environment and human health (Beerling et al., 2020; Haque et al., 2020a). Porewater concentrations were compared to surface water quality thresholds for nickel (25 µg/L) and total chromium (1 µg/L), emplaced by the Ontario Ministry of the Environment (MOE, 1979) and the Canadian Council of Ministers of the Environment (CCME, 1999), respectively, to evaluate the safety of the kimberlite residues.

The Gahcho Kué residues exceed the average kimberlite Ni content and are below the Cr average yet have values exceeding the average for basalt (Figure 10B). Reactivity assessments determined that Cr release from the 100GK sample was consistently within water quality regulations, while Ni concentrations exceeded this regulation by ~65 µg/L (Figure 3). In the field experiment, Ni and Cr levels in the amended plots exceeded control soils, yet the maximum concentrations of 11.3 and 0.94 µg/L, respectively, remained below surface water quality thresholds (Figures 7F,G).

Initial environmental assessments of reference lakes prior to the construction of the Gahcho Kué mine reported Ni and Cr levels well below 1 µg/L (Golder Associates, 2014). Routine water quality monitoring has since reported slightly elevated Ni concentrations (5 µg/L) and Cr concentrations below 1 µg/L in FPK residue contact waters (De Beers Canada Inc., 2020b). Humidity cell tests, used routinely in mine waste geochemical characterization, corroborate these results with reports of CPK and FPK exhibiting low metal leaching potential (De Beers Canada Inc., 2021). This is further supported by the minimal Ni and Cr relative to the whole rock geochemical content (Figure 10B) that became mobile from the weathering of the kimberlite residues in the experimental plots. The disparity in metal release, with Cr being ~2.5 orders of magnitude lower than Ni, is likely attributed to greater chances for Ni substitution (e.g., Mg in olivine) and less available sites for Cr replacement (e.g., Al in pyroxene; Kierczak et al., 2021). Cr release from the pure residues sample (100GK) leachates were also within the blank range (0.2 µg/L ± 0.1) suggesting no Cr was released. While the alkaline pH of these environments may prevent the mobility of these deleterious metals in waters, Ni can be adsorbed and retained in sediments for longer periods (Vienne et al., 2022). Metal accumulation is potentially facilitated by additional dosages and the adsorptive properties of clays present in the kimberlite residues (Pogge von Strandmann et al., 2022). Nevertheless, even with high dosages (e.g., 400 t/ha), Ni and Cr remained below strict Canadian water quality guidelines (MOE, 1979; CCME, 1999).

Soil accumulation ($CCME_{agricultural/residential}$: 45 mg Ni/kg, 64 mg Cr/kg; $CCME_{commercial/industrial}$: 89 mg Ni/kg, 87 mg Cr/kg; CCME, 2006, 2015) was not assessed in this experiment. Haque et al. (2020a) reviewed metal leaching data related to ERW projects and proposed 113 t/ha as a maximum application for olivine powder containing ~3 g Ni per kg olivine (3,200 t/ha for olivine containing 150 mg Cr per kg olivine). Renforth et al. (2015) performed a similar calculation based on empirical data from olivine-amended soil columns, considering the density of soil and an accumulation depth of 20 cm, reporting a maximum dosage of 95 t/ha to satisfy a Ni threshold of ~100 mg Ni/kg soil, which is near the $\text{CCME}_{\text{commercial/industrial}}$ land use threshold. Compared to the kimberlite residues in this study (1.2 g Ni/kg and 0.7 g Cr/kg), the initially high dosages applied (100 and 200 t/ha) do not pose a risk under Canadian metal accumulation guidelines; however, continued monitoring is required to assess the safety of the cumulative dosage on the K10+30 plot (400 t/ha). Dupla et al. (2023) modeled toxic metal accumulation in soils from ultramafic rock (~3 g Ni/kg) applied annually (40 t/ha), reporting exceedances of Canadian thresholds in <5 years. However, these soil cumulation values are calculated from the entire quantity of metals within a sample after digestion and do not consider the low leaching potential from resistant phases and immobility of some metals in neutral pH environments. Rapid exceedances of toxic element thresholds primarily occur in acidic conditions, such as a pH value of 4.2 used by Dupla et al. (2023), facilitating the mobility of metals. Instead, circumneutral soils that promote buffering HCO_3^- ions are sufficient for CDR while preventing metal leaching.

The addition of mineral feedstocks can replenish essential macronutrients (e.g., P and K), improving vegetation health and yield (Swoboda et al., 2022). The gradual release of nutrients from amendment weathering can aid revegetation efforts, offering a sustainable alternative to costly fertilizers (Mohammed et al., 2014). Although Gahcho Kué residues are below global kimberlite P averages, they notably exceed the K average due to microcline and phlogopite abundance comprising 27.2 wt.% of the kimberlite (Figure 10C; Table 1). PCA of the batch leach data indicated that P originated from soil influence, and as XRD indicated an absence of phosphate minerals [e.g., apatite $(Ca_5(PO_4)_3(OH, F, Cl))$] and geochemical data showed similarly low percentages of P-bearing oxides compared to soils (Table 2), amending soils with kimberlite residues had no effect on P levels and remained consistent with background levels (Supplementary Figure S2). Whereas PCA of leachates showed a strong correlation between K and kimberlite content, leaching 25.8% of the initial K concentrations (Figure 4; Table 3). The long-term potential for K input is substantial, with concentrations remaining elevated over multiple monitoring periods without the need for re-amendment (e.g., K20; Figure 7E). K-feldspars (e.g., microcline) compose 12.1 wt.% of the kimberlite residues suggesting a slow-releasing K source; however, K bound to K-feldspars are relatively inert compared to K fertilizers (Bakken et al., 2000). To contrast, Manning et al. (2017) report that K-feldspar rich rock powders would likely perform as a slow-inputting K source, while phlogopite containing rocks, like these kimberlite residues (15.5 wt.%), successfully impact crop yield on par with KCl fertilizer.

6.6 Implications for enhanced rock weathering using mine wastes

6.6.1 On-site ERW

The Gahcho Kué Diamond Mine plans to process 44.3 Mt of kimberlite ore, yielding 28.8 Mt of coarse processed kimberlite (CPK) and grits (0.25–6 mm), and 15.5 Mt of fine processed kimberlite (FPK) (De Beers Canada Inc., 2020a). Operational activities involve transporting FPK as a slurry to a containment facility with a capacity of 6.1 Mt, while CPK is stockpiled at a second facility capable of holding up to 27 Mt (De Beers Canada Inc., 2024). As part of their closure plan for 2030, FPK will be used as backfill in the Hearne open pit, with any residual FPK in the containment facility capped to mitigate further reactions (De Beers Canada Inc., 2024). Gahcho Kué operations may emit ~1.9 Mt CO_2e from construction to mine closure (~16 years), primarily from diesel-powered generators (De Beers Canada Inc., 2024). This estimate is based on the reported CO_2e emissions of ~723 kt from 2015 to 2021 and the average annual ~130 kt CO_2e generated during full operation (De Beers Canada Inc., 2023). As Gahcho Kué nears closure, mine production is likely to decline, and therefore, emissions will decrease; thus, 1.9 Mt CO_2e is an upper estimate of potential emissions.

Novel mine waste management practices offer the potential to optimize CDR during operation and improve site remediation post-closure. Conventional impoundments effectively store megatonnes of mine wastes, preventing weathering, leaching, and CO_2 reactions. In contrast, the aim of ERW is to widely distribute rock powders to optimize exposure. For instance, at the Mount Keith Nickel Mine in Western Australia, Wilson et al. (2014) recommended tailings management practices, such as employing thinner slurry flows and larger impoundments to enhance surface exposure and facilitate brucite $[Mg(OH)_2]$ carbonation. At Gahcho Kué, assuming complete carbonation of CaO and MgO and subsequent carbonate mineral formation at a 1:1 molar ratio with carbon, the estimated amount of FPK produced over the life of the mine has the potential to remove 5.0 Mt of CO_2, 9.9 Mt of CO_2 if considering solubility trapping. Thus, residue management that facilitates reactions with CO_2 could offset the anticipated emissions at Gahcho Kué by 2–5 × through the weathering of their FPK only.

Post-closure remediation is necessary to mitigate environmental and community impacts (Komljenovic et al., 2020); however, measures preventing further reactions in mafic and ultramafic mine wastes can hinder passive carbonation (Wilson et al., 2011). Exploring alternative storage methods for environmentally safe mine wastes could instead enhance CDR while addressing waste management concerns (Allory et al., 2022; Bullock et al., 2023a; Ruiz et al., 2023). One such approach involves building technosols from mine wastes, which have demonstrated potential for promoting vegetation growth, improving soil stability and fertility, and increasing CDR (Weiler et al., 2024). In this study, kimberlite residues demonstrated a readily available supply of K (Figure 7E), supporting potential reclamation of mine sites using an on-site material. Another example, Miller and Naeth (2017) showed that a 25:75 mixture of kimberlite residues from the Diavik Diamond Mine (Canada) and lakebed sediment successfully supported revegetation, recommending the addition of coarser materials, such as waste rock or coarse residues, to improve macropore storage and support seed germination. Co-disposal of coarse and fine kimberlite residues has also demonstrated residue stabilization through cementation of finer particles (<63 μm) between larger clasts, with Lockhart et al. (2024) recommending modified coarse:fine ratios to subsequently support carbon mineralization.

At the Gahcho Kué mine, De Beers plans to repurpose overburden and lakebed sediment as a substrate for revegetation (De Beers Canada Inc., 2024). This ~1,300 ha site also presents an opportunity for ERW, utilizing processed residues to rehabilitate disturbed lands. Reclamation efforts also include loosening compacted zones (e.g., roads) that make up 160 ha of the mine to encourage vegetation establishment (De Beers Canada Inc., 2024), providing opportunities to integrate residues with soil to include CDR benefits while promoting plant growth. Additionally, the amount of land available on-site allows for optimal ratios of residues to soil, with decreased CDR efficiency as a result of higher rock-to-water ratios demonstrated in this study. For example, porewaters from the K10+30 plot (400 t/ha) became saturated with respect to lizardite after reamendment, thereby inhibiting further dissolution (Supplementary Table S2). The K20 plot, treated with a dosage of 200 t/ha, achieved comparable CDR to the K10+30 plot after 3 years, highlighting the efficacy of lower dosage rates. Longer on-site field trials are warranted to monitor feedstock weathering and gradual silicate dissolution, particularly at lower rock-to-water ratios. Incorporating residues into these remediation strategies would facilitate long-term CDR, offsetting historical GHG emissions from operations long after mine closure.

6.6.2 Off-site ERW

The vast reserve of known kimberlite occurrences (~6,500) worldwide presents a significant opportunity for carbon sequestration, but only ~1,000 host macro-diamonds of economic value that are feasible for extraction (Kjarsgaard et al., 2022). The global production of diamonds from 1854 to 2019 is estimated at 5.9 billion carats (Kjarsgaard et al., 2022), which would have generated approximately 3.9 Gt of kimberlite residues assuming an average ore grade of ~1.5 carats per tonne kimberlite (Gurney et al., 2005). Based on the average kimberlite oxide contents from the GEOROC database (see see text footnote 1; DIGIS Team, 2025), and using the Steinour equation, the global quantity of kimberlite residues could remove 545–618 kg CO_2/t or just over 2 Gt of CO_2. These residues would include fine and coarse fractions located at active and closed diamond mines in countries such as Angola, Australia, Botswana, Brazil, Canada, China, Democratic Republic of the Congo, Lesotho, Russia, Sierra Leone, South Africa, Tanzania, and Zimbabwe (Kjarsgaard et al., 2022). Existing mine residues are readily available fine-grained feedstocks that offer a pathway toward achieving net-neutral mining operations and for post-closure remediation efforts (Bullock et al., 2021).

Repurposing industrial waste within the circular economy framework presents an opportunity to optimize global CDR through ERW, while addressing waste management challenges. Renforth et al. (2011) acknowledge that the prime limitation for sufficient geochemical CDR is material availability, highlighting the opportunity for managing disposed silicate waste (e.g., mine waste, cement dust, and slag) for CDR. Globally, 7–17 Gt of industrial silicate waste is produced annually and largely stockpiled, with Manning and Renforth (2013) equating this source of readily available feedstock to a solubility trapping capacity of 1.2–2.0 Gt CO_2/year.

Applications of environmentally safe industrial wastes have proven effective in remediating degraded soils from mining and agriculture (Baragaño et al., 2019; Ramos et al., 2020, 2021; Díaz-Piloneta et al., 2022), with recent consideration for CDR projects (Bullock et al., 2023a). Steel slag, for instance, contains Ca- and Mg-silicates, free lime (CaO), portlandite [$Ca(OH)_2$], and abundant micronutrients, making it a viable industrial waste for CDR (Reddy et al., 2019), with large quantities available (Díaz-Piloneta et al., 2022). Crushed returned concrete has shown promise as a soil amendment, achieving rapid soil neutralization and maximum CDR rates of ~0.5 t CO_2/ha over 10 months due to its reactive Ca phases [e.g., $Ca(OH)_2$; McDermott et al., 2024]. ERW operations tend to use quarry by-products from mafic aggregate mining as they are discarded without prior chemical processing (Ramos et al., 2020), and contain relatively fast-weathering silicate phases (e.g., dunite residues: 20–35 wt.% olivine; Baragaño et al., 2019). Although common misconceptions regarding sulfide and metal concentrations may undervalue relatively environmentally safe mine wastes such as kimberlite residues from green practices, there is a broad opportunity, alongside other industrial by-products, to repurpose such materials for CDR.

The CDR rates determined in this study using kimberlite residues are within the range of rates for basalt ERW field experiments and trials range (0.05–17.6 t CO_2/ha/year; Manning and Renforth, 2013; Larkin et al., 2022; Harrington et al., 2023; Holzer et al., 2023; Paessler et al., 2023; Beerling et al., 2024; Honvault et al., 2024) which varies by orders of magnitude (Power et al., 2025). This field experiment applied kimberlite residues off-site yielding similar solubility trapping rates to the basalt distributed in Malaysia reported by Larkin et al. (2022), although basalt dosages were considerably lower (50 t/ha).

It is important to acknowledge that the kimberlite CDR rates measured in this study were influenced by specific weathering conditions subject to a continental climate and calcareous soil, which differs from the tropical climate of Malaysia and the subarctic climate at the Gahcho Kué mine and the faster weathering rates that would have been achieved in more acidic soils. Moreover, CDR rates for other kimberlites would vary depending on their mine site environment and near-by viable lands for off-site application, such as the farmland adjacent to the Voorspoed mine and desert surrounding the Venetia mine in South Africa, or the diverse conservation parks containing the Jwaneng and Orapa mines in Botswana. Thus, accurate measurements and monitoring of field rates using instrumentation similar to the monitoring plots in this study is recommended for an ERW deployment.

Transporting mine residues off-site raises legal concerns regarding air and water quality and may encounter opposition from local authorities (Webb, 2020). The limitations governing the relocation of mine waste for ERW in the United States were evaluated by Webb (2020) who highlighted the potential for managing the application of artificial silicates (e.g., mine waste) to designated lands for a specific purpose (e.g., ERW) within waste disposal regulations. This approach could be viable provided there is sufficient buffer land between the placement of industrial wastes and nearby agricultural fields (Webb, 2020); although, basalt—a waste product from quarries—is already widely applied to croplands for ERW (Beerling et al., 2024), and agriculture is not present in these often-remote sites. Still, amending existing regulations specifically for ERW is recommended by Webb (2020).

The use of rock feedstocks on croplands for agricultural benefits and CDR (Beerling et al., 2020) has outweighed consideration of their application in industrially degraded lands, due to their substantial landcover and established infrastructure for spreading fertilizers (Power et al., 2024). Repurposing and depositing mine residues offsite, depending on the land use, would require case-specific permits with varying thresholds of acceptable cation leaching and soil impacts. Thus, the establishment of long-term monitoring stations to directly measure feedstock weathering must be incorporated into these regulations. Protocols are being established for geochemical CDR projects in various settings including ERW on agricultural fields (Sutherland et al., 2023—Isometric) and ex-situ mineralization applicable to mine sites (Savage et al., 2024—Isometric) providing procedural requirements and considerations when quantifying CDR rates. By adhering to robust regulatory frameworks and implementing thorough monitoring protocols, mine residues and other industrial wastes can be managed responsibly and sustainably while maximizing their potential for carbon removal.

7 Conclusion

Over 3 years, kimberlite residues from Gahcho Kué sequestered 1.4 and 1.3 t CO_2/ha via solubility trapping at application rates of 400 and 200 t/ha, respectively. Shallow porewater samples for both amended plots exhibited clear evidence of elevated DIC and alkalinity relative to the control, with supporting $^{13}C_{DIC}$ compositions indicating that the sequestered CO_2 originated from organic sources via soil respiration. Throughout the experiment, Ni and Cr concentrations remained within safe limits in porewaters of the amended plots, while porewaters became enriched in K following amendments, validating kimberlite residues as a viable soil amendment.

This study demonstrates the efficacy of shallow water sampling and soil moisture monitoring in tracking CO_2 removed through solubility trapping. Using a water budget approach and analyzing DIC in porewaters, we quantified the generation of HCO_3^- from weathering kimberlite residues relative to background signals. Importantly, we differentiated carbonate and silicate weathering contributions based on cation loadings. The choice of cations to track was determined through an initial reactivity assessment of the residues, identifying cations most indicative of kimberlite and soil weathering. We highlighted the challenges of detecting carbon removal via CO_2 fluxes, given the overwhelming effluxes from soil respiration, and the unreliability of TIC measurements for quantifying mineral trapping in calcareous soils.

We encourage the mining industry to consider incorporating ERW of environmentally safe residues into management practices to sustain reactions between residues and CO_2 during operation and post-closure. Dispersing kimberlite residues on-site as a soil substrate for mine remediation and off-site as a soil remineralizer would minimize containment and land reclamation costs, while aiding the scaling up of ERW by utilizing abundant mineral waste.

Data availability statement

The original contributions presented in the study are included in the article/Supplementary material, further inquiries can be directed to the corresponding author.

Author contributions

ZS: Data curation, Investigation, Methodology, Visualization, Writing – original draft, Writing – review & editing, Formal analysis, Funding acquisition. KR: Data curation, Investigation, Methodology, Writing – review & editing, Validation. IP: Conceptualization, Formal analysis, Funding acquisition, Methodology, Visualization, Writing – review & editing, Project administration, Resources, Supervision. CP: Visualization, Writing – review & editing, Formal analysis, Validation.

Funding

The author(s) declare that financial support was received for the research and/or publication of this article. This research was supported by an Ontario Graduate Scholarship awarded to ZS and a Natural Sciences and Engineering Research Council of Canada Discovery grant (RGPIN-2024-03734) and Canada Research Chair (CRC-2021-00338) to IP.

Acknowledgments

We thank De Beers Group Services for providing the kimberlite residues. Porewater chemistry was partly analyzed at the Water Quality Centre (Trent University), and we thank Karla Newman for her technical support and guidance. We also appreciate the thought-provoking conversations had with colleagues from the PowerGeolab. We thank the editor for handling our manuscript and the reviewers for their insightful and helpful comments.

Conflict of interest

The authors declare that the research was conducted in the absence of any commercial or financial relationships that could be construed as a potential conflict of interest.

Generative AI statement

The authors declare that no Gen AI was used in the creation of this manuscript.

Publisher's note

Supplementary material

The Supplementary material for this article can be found online at: https://www.frontiersin.org/articles/10.3389/fclim.2025.1592626/full#supplementary-material

References

Allory, V., Séré, G., and Ouvrard, S. (2022). A meta-analysis of carbon content and stocks in technosols and identification of the main governing factors. *Eur. J. Soil Sci.* 73, 1–17. doi: 10.1111/ejss.13141

Almaraz, M., Bingham, N. L., Holzer, I. O., Geoghegan, E. K., Goertzen, H., Sohng, J., et al. (2022). Methods for determining the CO_2 removal capacity of enhanced weathering in agronomic settings. *Front. Clim.* 4:970429. doi: 10.3389/fclim.2022.970429

Amann, T., and Hartmann, J. (2022). Carbon accounting for enhanced weathering. *Front. Clim.* 4:849948. doi: 10.3389/fclim.2022.849948

Amann, T., Hartmann, J., Struyf, E., De Oliveira Garcia, W., Fischer, E. K., Janssens, I., et al. (2020). Enhanced weathering and related element fluxes - a cropland mesocosm approach. *Biogeosciences* 17, 103–119. doi: 10.5194/bg-17-103-2020

Bakken, A. K., Gautneb, H., Sveistrup, T., and Myhr, K. (2000). Crushed rocks and mine tailings applied as K fertilizers on grassland. *Nutr. Cycl. Agroecosyst.* 56, 53–57. doi: 10.1023/A:1009709914578

Baragaño, D., Forján, R., Aguado, J. M. M., Martino, M. C., García, P. D., Rubio, J. M., et al. (2019). Reuse of dunite mining waste and subproducts for the stabilization of metal(oid)s in polluted soils. *Fortschr. Mineral.* 9, 1–11. doi: 10.3390/min9080481

Beerling, D. J., Epihov, D. Z., Kantola, I. B., Masters, M. D., Reershemius, T., Planavsky, N. J., et al. (2024). Enhanced weathering in the US Corn Belt delivers carbon removal with agronomic benefits. *Proc. Natl. Acad. Sci. USA* 121:e2319436121. doi: 10.1073/pnas.2319436121

Beerling, D. J., Kantzas, E. P., Lomas, M. R., Wade, P., Eufrasio, R. M., Renforth, P., et al. (2020). Potential for large-scale CO_2 removal via enhanced rock weathering with croplands. *Nature* 583, 242–248. doi: 10.1038/s41586-020-2448-9

Beerling, D. J., Leake, J. R., Long, S. P., Scholes, J. D., Ton, J., Nelson, P. N., et al. (2018). Farming with crops and rocks to address global climate, food and soil security. *Nat. Plants* 4, 138–147. doi: 10.1038/s41477-018-0108-y

Brantley, S. L., and Olsen, A. A. (2014). Reaction kinetics of primary rock-forming minerals under ambient conditions. Oxford: Elsevier.

Brown, D. M., Dadfar, H., Fallow, D. J., Gordon, R. J., Lauzon, J. D., and Parkin, G. W. (2013). Temporal and spatial variability of water surplus in Ontario, Canada. *ISRN Soil Sci.* 2013, 1–7. doi: 10.1155/2013/362895

Brunauer, S., Emmett, P. H., and Teller, E. (1938). Adsorption of gases in multimolecular layers. *J. Am. Chem. Soc.* 60, 309–319. doi: 10.1021/ja01269a023

Bullock, L. A., Fernandez-Turiel, J. L., and Benavente, D. (2023a). Experimental investigation of multiple industrial wastes for carbon dioxide removal strategies. *Int. J. Greenhouse Gas Control* 129:103990. doi: 10.1016/j.ijggc.2023.103990

Bullock, L. A., James, R. H., Matter, J., Renforth, P., and Teagle, D. A. H. (2021). Global carbon dioxide removal potential of waste materials from metal and diamond mining. *Front. Clim.* 3:694175. doi: 10.3389/fclim.2021.694175

Bullock, L. A., Nkosi, Z., Vele, M., and Amponsah-Dacosta, M. (2023b). Catalogue of south African mine tailings for geochemical carbon dioxide removal purposes. *Int. J. Greenhouse Gas Control* 124:103844. doi: 10.1016/j.ijggc.2023.103844

Calabrese, S., Wild, B., Bertagni, M. B., Bourg, I. C., White, C., Aburto, F., et al. (2022). Nano- to global-scale uncertainties in terrestrial enhanced weathering. *Environ. Sci. Technol.* 56, 15261–15272. doi: 10.1021/acs.est.2c03163

CCME (1999). Canadian water quality guidelines for the protection of aquatic life. National Harbor, MD: CCME.

CCME (2006). A protocol for the derivation of environmental and human health soil quality guidelines. National Harbor, MD: CCME.

CCME (2015). Canadian soil quality guidelines for the protection of environmental and human health: Nickel. National Harbor, MD: CCME.

Clarkson, M. O., Larkin, C. S., Swoboda, P., Reershemius, T., Suhrhoff, T. J., Maesano, C. N., et al. (2024). A review of measurement for quantification of carbon dioxide removal by enhanced weathering in soil. *Front. Clim.* 6:1345224. doi: 10.3389/fclim.2024.1345224

Daval, D., Hellmann, R., Martinez, I., Gangloff, S., and Guyot, F. (2013). Lizardite serpentine dissolution kinetics as a function of pH and temperature, including effects of elevated pCO_2. *Chem. Geol.* 351, 245–256. doi: 10.1016/j.chemgeo.2013.05.020

De Beers Canada Inc. (2020a). Gahcho Kué mine: geochemical characterization plan version 4.2. Calgary, AB: De Beers Canada Inc.

De Beers Canada Inc. (2020b). Gahcho Kué mine: Monthly surveillance network program report (MV2005L2-0015). Calgary, AB: De Beers Canada Inc.

De Beers Canada Inc. (2021). Gahcho Kué mine: processed kimberlite and mine rock management plan version 7.2. Calgary, AB: De Beers Canada Inc.

De Beers Canada Inc. (2023). Gahcho Kué mine: 2021 annual air quality report. Calgary, AB: De Beers Canada Inc.

De Beers Canada Inc. (2024). Gahcho Kué. Mine: Interim Closure and Reclamation Plan. Calgary, AB: De Beers Canada Inc.

Díaz-Piloneta, M., Ortega-Fernández, F., Terrados-Cristos, M., and Valeriano Álvarez-Cabal, J. (2022). Application of steel slag for degraded land remediation. *Land* 11:224. doi: 10.3390/land11020224

Dietzen, C., and Rosing, M. T. (2023). Quantification of CO_2 uptake by enhanced weathering of silicate minerals applied to acidic soils. *Int. J. Greenhouse Gas Control* 125:103872. doi: 10.1016/j.ijggc.2023.103872

DIGIS Team (2025). GEOROC compilation: rock types. *GRO.data* 10, 1–15. doi: 10.25625/2JETOA

Dubois, K. D., Lee, D., and Veizer, J. (2010). Isotopic constraints on alkalinity, dissolved organic carbon, and atmospheric carbon dioxide fluxes in the Mississippi River. *J. Geophys. Res.* 115:1102. doi: 10.1029/2009JG001102

Dupla, X., Möller, B., Baveye, P. C., and Grand, S. (2023). Potential accumulation of toxic trace elements in soils during enhanced rock weathering. *Eur. J. Soil Sci.* 74:e13343. doi: 10.1111/ejss.13343

ECCC (2021). Canadian climate normals 1991–2020. Decatur, MI: ECCC.

Farhang, F., Rayson, M., Brent, G., Hodgins, T., Stockenhuber, M., and Kennedy, E. (2017). Insights into the dissolution kinetics of thermally activated serpentine for CO_2 sequestration. *Chem. Eng. J.* 330, 1174–1186. doi: 10.1016/j.cej.2017.08.073

Giuliani, A., Phillips, D., Kamenetsky, V. S., Fiorentini, M. L., Farquhar, J., and Kendrick, M. A. (2014). Stable isotope (C, O, S) compositions of volatile-rich minerals in kimberlites: a review. *Chem. Geol.* 375, 61–83. doi: 10.1016/j.chemgeo.2014.03.003

Golder Associates (2014). Gahcho Kué project: 2013 supplemental monitoring report-water quality and sediment quality-core, reference, and raised lakes. Toronto, ON: Golder Associates.

Goll, D. S., Ciais, P., Amann, T., Buermann, W., Chang, J., Eker, S., et al. (2021). Potential CO_2 removal from enhanced weathering by ecosystem responses to powdered rock. *Nat. Geosci.* 14, 545–549. doi: 10.1038/s41561-021-00798-x

Gunnarsen, K. C., Jensen, L. S., Rosing, M. T., and Dietzen, C. (2023). Greenlandic glacial rock flour improves crop yield in organic agricultural production. *Nutr. Cycl. Agroecosyst.* 126, 51–66. doi: 10.1007/s10705-023-10274-0

Guo, F., Wang, Y., Zhu, H., Zhang, C., Sun, H., Yang, J., et al. (2023). Crop productivity and soil inorganic carbon change mediated by enhanced rock weathering in farmland: a comparative field analysis of multi-agroclimatic regions in Central China. *Agric. Syst.* 210:103691. doi: 10.1016/j.agsy.2023.103691

Gurney, J. J., Helmstaedt, H. H., Le Roex, A. P., Nowicki, T. E., Richardson, S. H., and Westerlund, K. J. (2005). Diamonds: crustal distribution and formation processes in time and space and an integrated deposit model. *Econ. Geol.* 11, 143–177. doi: 10.5382/AV100.07

Haque, F., Chiang, Y. W., and Santos, R. M. (2020a). Risk assessment of Ni, Cr, and Si release from alkaline minerals during enhanced weathering. *Open Agric* 5, 166–175. doi: 10.1515/opag-2020-0016

Haque, F., Santos, R. M., and Chiang, Y. W. (2020b). CO_2 sequestration by wollastonite-amended agricultural soils – an Ontario field study. *Int. J. Greenhouse Gas Control* 97:103017. doi: 10.1016/j.ijggc.2020.103017

Haque, F., Santos, R. M., Dutta, A., Thimmanagari, M., and Chiang, Y. W. (2019). Co-benefits of wollastonite weathering in agriculture: CO_2 sequestration and promoted plant growth. *ACS Omega* 4, 1425–1433. doi: 10.1021/acsomega.8b02477

Harrington, K. J., Hilton, R. G., and Henderson, G. M. (2023). Implications of the riverine response to enhanced weathering for CO_2 removal in the UK. *Appl. Geochem.* 152:105643. doi: 10.1016/j.apgeochem.2023.105643

Heřmanská, M., Voigt, M. J., Marieni, C., Declercq, J., and Oelkers, E. H. (2023). A comprehensive and consistent mineral dissolution rate database: part II: secondary silicate minerals. *Chem. Geol.* 636:121632. doi: 10.1016/j.chemgeo.2023.121632

Hetman, C. M., Scott Smith, B. H., Paul, J. L., and Winter, F. (2004). Geology of the Gahcho Kué kimberlite pipes, NWT, Canada: root to diatreme magmatic transition zones. *Lithos* 76, 51–74. doi: 10.1016/j.lithos.2004.03.051

Hoegh-Guldberg, O., Jacob, D., Taylor, M., Bindi, M., Brown, S., Camilloni, I., et al. (2018). "Impacts of 1.5°C of global warming on natural and human systems" in Global warming of 1.5°C. An IPCC special report on the impacts of global warming of 1.5°C above pre-industrial levels and related global greenhouse gas emission pathways, in the context of strengthening the global response to the threat of climate change, sustainable development, and efforts to eradicate poverty. eds. V. Masson-Delmotte, P. Zhai, H.-O. Pörtner, D. Roberts, J. Skea and P. R. Shukla (Geneva: IPCC).

Holzer, I. O., Nocco, M. A., and Houlton, B. Z. (2023). Direct evidence for atmospheric carbon dioxide removal via enhanced weathering in cropland soil. *Environ. Res. Commun.* 5:101004. doi: 10.1088/2515-7620/acfd89

Honvault, N., Tiouchichine, M. L., Sauze, J., Piel, C., Landais, D., Devidal, S., et al. (2024). Additive effects of basalt enhanced weathering and biochar co-application on carbon sequestration, soil nutrient status and plant performance in a mesocosm experiment. *Appl. Geochem.* 169:106054. doi: 10.1016/j.apgeochem.2024.106054

Iff, N., Renforth, P., and Pogge von Strandmann, P. A. E. (2024). The dissolution of olivine added to soil at 32°C: the fate of weathering products and its implications for enhanced weathering at different temperatures. *Front. Clim.* 6:1252210. doi: 10.3389/fclim.2024.1252210

Jones, R., Fox, M. G., and Marsh, J. S. (2002). Trent nature areas: Geological history. Peterborough ON: Nature Areas Committee, Trent University.

Jones, T. R., Poitras, J., Gagen, E., Paterson, D. J., and Southam, G. (2023). Accelerated mineral bio-carbonation of coarse residue kimberlite material by inoculation with photosynthetic microbial mats. *Geochem. Trans.* 24:1. doi: 10.1186/s12932-023-00082-4

Kantola, I. B., Blanc-Betes, E., Masters, M. D., Chang, E., Marklein, A., Moore, C. E., et al. (2023). Improved net carbon budgets in the US Midwest through direct measured impacts of enhanced weathering. *Glob. Chang. Biol.* 29, 7012–7028. doi: 10.1111/gcb.16903

Kanzaki, Y., Planavsky, N. J., Zhang, S., Jordan, J., and Reinhard, C. T. (2024). Soil cation storage as a key control on the timescales of carbon dioxide removal through enhanced weathering. *Earths Future* 22, 1–19. doi: 10.22541/essoar.172163224.49852060/v1

Kelland, M. E., Wade, P. W., Lewis, A. L., Taylor, L. L., Sarkar, B., Andrews, M. G., et al. (2020). Increased yield and CO_2 sequestration potential with the C4 cereal Sorghum bicolor cultivated in basaltic rock dust-amended agricultural soil. *Glob. Chang. Biol.* 26, 3658–3676. doi: 10.1111/gcb.15089

Kierczak, J., Pietranik, A., and Pędziwiatr, A. (2021). Ultramafic geoecosystems as a natural source of Ni, Cr, and co to the environment: a review. *Sci. Total Environ.* 755:142620. doi: 10.1016/j.scitotenv.2020.142620

Kjarsgaard, B. A., de Wit, M., Heaman, L. M., Pearson, D. G., Stiefenhofer, J., Janusczcak, N., et al. (2022). A review of the geology of global diamond mines and deposits. *Rev. Mineral. Geochem.* 88, 1–117. doi: 10.2138/rmg.2022.88.01

Knapp, W. J., Stevenson, E. I., Renforth, P., Ascough, P. L., Knight, A. C. G., Bridgestock, L., et al. (2023). Quantifying CO_2 removal at enhanced weathering sites: a multiproxy approach. *Environ. Sci. Technol.* 57, 9854–9864. doi: 10.1021/acs.est.3c03757

Knapp, W. J., and Tipper, E. T. (2022). The efficacy of enhancing carbonate weathering for carbon dioxide sequestration. *Front. Clim.* 4:928215. doi: 10.3389/fclim.2022.928215

Komljenovic, D., Stojanovic, L., Malbasic, V., and Lukic, A. (2020). A resilience-based approach in managing the closure and abandonment of large mine tailing ponds. *Int. J. Min. Sci. Technol.* 30, 737–746. doi: 10.1016/j.ijmst.2020.05.007

Larkin, C. S., Andrews, G. M., Pearce, C. R., Yeong, K. L., Beerling, D. J., Bellamy, J., et al. (2022). Quantification of CO_2 removal in a large-scale enhanced weathering field trial on an oil palm plantation in Sabah, Malaysia. *Front. Clim.* 4:959229. doi: 10.3389/fclim.2022.959229

Lewis, A. L., Sarkar, B., Wade, P., Kemp, S. J., Hodson, M. E., Taylor, L. L., et al. (2021). Effects of mineralogy, chemistry and physical properties of basalts on carbon capture potential and plant-nutrient element release via enhanced weathering. *Appl. Geochem.* 132:105023. doi: 10.1016/j.apgeochem.2021.105023

Liu, Z., Dreybrodt, W., and Liu, H. (2011). Atmospheric CO_2 sink: silicate weathering or carbonate weathering? *Appl. Geochem.* 26, S292–S294. doi: 10.1016/j.apgeochem.2011.03.085

Lockhart, J. A., Power, I. M., Paulo, C., Stubbs, A. R., Zeyen, N., Wilson, S., et al. (2024). Weathering and cementation of historic kimberlite residues from South Africa: implications for residue stabilization and CO_2 sequestration. *Sci. Total Environ.* 955:177094. doi: 10.1016/j.scitotenv.2024.177094

Lu, X., Carroll, K. J., Turvey, C. C., and Dipple, G. M. (2022). Rate and capacity of cation release from ultramafic mine tailings for carbon capture and storage. *Appl. Geochem.* 140:105285. doi: 10.1016/j.apgeochem.2022.105285

Manning, D. A. C., Baptista, J., Sanchez Limon, M., and Brandt, K. (2017). Testing the ability of plants to access potassium from framework silicate minerals. *Sci. Total Environ.* 574, 476–481. doi: 10.1016/j.scitotenv.2016.09.086

Manning, D. A. C., and Renforth, P. (2013). Passive sequestration of atmospheric CO_2 through coupled plant-mineral reactions in urban soils. *Environ. Sci. Technol.* 47, 135–141. doi: 10.1021/es301250j

Manning, D. A. C., Renforth, P., Lopez-Capel, E., Robertson, S., and Ghazireh, N. (2013). Carbonate precipitation in artificial soils produced from basaltic quarry fines and composts: an opportunity for passive carbon sequestration. *Int. J. Greenhouse Gas Control* 17, 309–317. doi: 10.1016/j.ijggc.2013.05.012

Maxbauer, D. P., and Yambing, J. R. (2022). Carbon sequestration by enhanced silicate weathering in agricultural soils. *Keck Geol. Consortium* 34, 1–5. doi: 10.18277/AKRSG.2022.34.03

McDermott, F., Barros, R., and Cooper, M. (2019). An investigation of waste basalt (quarry dust) as a soil amendment to sequester atmospheric CO_2. *Geophys. Res. Abstr.* 21:EGU2019-5908-1.

McDermott, F., Bryson, M., Magee, R., and van Acken, D. (2024). Enhanced weathering for CO_2 removal using carbonate-rich crushed returned concrete; a pilot study from SE Ireland. *Appl. Geochem.* 169:106056. doi: 10.1016/j.apgeochem.2024.106056

McDonald, D. T. E. (2023). Predicting and monitoring drainage chemistry during mineral weathering for CO_2 sequestration. Peterborough: Trent University.

McDonald, D. T. E., Power, I. M., Paulo, C., and Wilson, S. (2025). CO2 mineralization of kimberlite residues from the Gahcho Kué diamond mine, Northwest Territories, Canada. *Int. J. Greenhouse Gas Control* 144:104376. doi: 10.1016/j.ijggc.2025.104376

Mervine, E. M., Wilson, S. A., Power, I. M., Dipple, G. M., Turvey, C. C., Hamilton, J. L., et al. (2018). Potential for offsetting diamond mine carbon emissions through mineral carbonation of processed kimberlite: an assessment of De beers mine sites in South Africa and Canada. *Mineral. Petrol.* 112, 755–765. doi: 10.1007/s00710-018-0589-4

Miller, V. S., and Naeth, M. A. (2017). Amendments and substrates to develop anthroposols for northern mine reclamation. *Can. J. Soil Sci.* 97, 266–277. doi: 10.1139/cjss-2016-0145

MOE (1979). Rationale for the establishment of Ontario's provincial water quality objectives. New Delhi: MOE.

Mohammed, S. M. O., Brandt, K., Gray, N. D., White, M. L., and Manning, D. A. C. (2014). Comparison of silicate minerals as sources of potassium for plant nutrition in sandy soil. *Eur. J. Soil Sci.* 65, 653–662. doi: 10.1111/ejss.12172

Mook, W. G., Bommerson, J. C., and Staverman, W. H. (1974). Carbon isotope fractionation between dissolved bicarbonate and gaseous carbon dioxide. *Earth Planet. Sci. Lett.* 22, 169–176. doi: 10.1016/0012-821X(74)90078-8

Moosdorf, N., Renforth, P., and Hartmann, J. (2014). Carbon dioxide efficiency of terrestrial enhanced weathering. *Environ. Sci. Technol.* 48, 4809–4816. doi: 10.1021/es4052022

Oelkers, E. H., Declercq, J., Saldi, G. D., Gislason, S. R., and Schott, J. (2018). Olivine dissolution rates: a critical review. *Chem. Geol.* 500, 1–19. doi: 10.1016/j.chemgeo.2018.10.008

Oelkers, E. H., Gislason, S. R., and Matter, J. (2008). Mineral carbonation of CO_2. *Elements* 4, 333–337. doi: 10.2113/gselements.4.5.333

Oh, N. H., and Raymond, P. A. (2006). Contribution of agricultural liming to riverine bicarbonate export and CO_2 sequestration in the Ohio River basin. *Global Biogeochem. Cycles* 20:2565. doi: 10.1029/2005GB002565

Paessler, D., Steffens, R., Hammes, J., and Smet, I. (2023). Monitoring CO_2 concentrations in soil gas: a novel MRV approach for cropland-based ERW? Available online at: www.carbon-drawdown.de (Accessed May 29, 2023).

Palandri, J. L., and Kharaka, Y. K. (2004). A compilation of rate parameters of water-mineral interaction kinetics for application to geochemical modeling. Denver: US Geological Survey.

Parkhurst, D., and Appelo, C. (2013). Description of input and examples for PHREEQC version 3-a computer program for speciation, batch-reaction, one-dimensional transport, and inverse geochemical calculations. Available online at: http://www.hydrochemistry.eu (Accessed January 1, 2023).

Parkin, G. W., Wagner-Riddle, C., Fallow, D. J., and Brown, D. M. (1999). Estimated seasonal and annual water surplus in Ontario. *Canadian Water Res. J.* 24, 277–292. doi: 10.4296/cwrj2404277

Paulo, C., Power, I. M., Stubbs, A. R., Wang, B., Zeyen, N., and Wilson, S. A. (2021). Evaluating feedstocks for carbon dioxide removal by enhanced rock weathering and CO_2 mineralization. *Appl. Geochem.* 129:104955. doi: 10.1016/j.apgeochem.2021.104955

Paulo, C., Power, I. M., Zeyen, N., Wang, B., and Wilson, S. A. (2023). Geochemical modeling of CO_2 sequestration in ultramafic mine wastes from Australia, Canada, and South Africa: implications for carbon accounting and monitoring. *Appl. Geochem.* 152:105630. doi: 10.1016/j.apgeochem.2023.105630

Pogge von Strandmann, P. A. E., Tooley, C., Mulders, J. J. P. A., and Renforth, P. (2022). The dissolution of olivine added to soil at 4°C: implications for enhanced weathering in cold regions. *Front. Clim.* 4:827698. doi: 10.3389/fclim.2022.827698

Pokrovsky, O. S., and Schott, J. (2000). Kinetics and mechanism of forsterite dissolution at 25°C and pH from 1 to 12. *Geochemica et Cosmochimica Acta* 64, 3313–3325. doi: 10.1016/S0016-7037(00)00434-8

Power, I. M., Harrison, A. L., Dipple, G. M., Wilson, S. A., Kelemen, P. B., Hitch, M., et al. (2013a). Carbon mineralization: from natural analogues to engineered systems. *Rev. Mineral. Geochem.* 77, 305–360. doi: 10.2138/rmg.2013.77.9

Power, I. M., Hatten, V. N. J., Guo, M., Schaffer, Z. R., Rausis, K., and Klyn-Hesselink, H. (2025). Are enhanced rock weathering rates overestimated? A few geochemical and mineralogical pitfalls. *Front. Clim.* 6:1510747. doi: 10.3389/fclim.2024.1510747

Power, I. M., Paulo, C., and Rausis, K. (2024). The mining industry's role in enhanced weathering and mineralization for CO_2 removal. *Environ. Sci. Technol.* 58, 43–53. doi: 10.1021/acs.est.3c05081

Power, I. M., Wilson, S. A., and Dipple, G. M. (2013b). Serpentinite carbonation for CO_2 sequestration. *Elements* 9, 115–121. doi: 10.2113/gselements.9.2.115

Rabenhorst, M. C., Wilding, L. P., and West, L. T. (1984). Identification of pedogenic carbonates using stable carbon isotope micro fabric analyses. *SoilGenesis Morphol. Classification* 48, 125–132. doi: 10.2136/sssaj1984.03615995004800010023x

Ramos, C. G., Dalmora, A. C., Kautzmann, R. M., Hower, J., Dotto, G. L., and Oliveira, L. F. S. (2021). Sustainable release of macronutrients to black oat and maize crops from organically-altered dacite rock powder. *Nat. Resour. Res.* 30, 1941–1953. doi: 10.1007/s11053-021-09862-0

Ramos, C. G., Dos Santos De Medeiros, D., Gomez, L., Oliveira, L. F. S., Schneider, I. A. H., and Kautzmann, R. M. (2020). Evaluation of soil re-mineralizer from by-product of volcanic rock mining: experimental proof using black oats and maize crops. *Nat. Resour. Res.* 29, 1583–1600. doi: 10.1007/s11053-019-09529-x

Reddy, K. R., Gopakumar, A., and Chetri, J. K. (2019). Critical review of applications of iron and steel slags for carbon sequestration and environmental remediation. *Rev. Environ. Sci. Biotechnol.* 18, 127–152. doi: 10.1007/s11157-018-09490-w

Renforth, P., Pogge von Strandmann, P. A. E., and Henderson, G. M. (2015). The dissolution of olivine added to soil: implications for enhanced weathering. *Appl. Geochem.* 61, 109–118. doi: 10.1016/j.apgeochem.2015.05.016

Renforth, P., Washbourne, C.-L., Taylder, J., and Manning, D. A. C. (2011). Silicate production and availability for mineral carbonation. *Environ. Sci. Technol.* 45, 2035–2041. doi: 10.1021/es103241w

Rollo, H. A., and Jamieson, H. E. (2006). Interaction of diamond mine waste and surface water in the Canadian Arctic. *Appl. Geochem.* 21, 1522–1538. doi: 10.1016/j.apgeochem.2006.05.008

Ruiz, F., Safanelli, J. L., Perlatti, F., Cherubin, M. R., Demattê, J. A. M., Pellegrino Cerri, C. E., et al. (2023). Constructing soils for climate-smart mining. *Commun Earth Environ* 4, 1–6. doi: 10.1038/s43247-023-00862-x

Savage, R., Sutherland, K., Holme, E., Tyne, R., Marsland, E., and Lu, X. (2024). Open system ex-situ mineralization v1.0 – Isometric. 1–167. Available online at: https://registry.isometric.com/protocol/open-system-ex-situ-mineralization/1.0 (Accessed January 16, 2025).

Schuiling, R. D., and Krijgsman, P. (2006). Enhanced weathering: an effective and cheap tool to sequester CO_2. *Clim. Chang.* 74, 349–354. doi: 10.1007/s10584-005-3485-y

Schulte, P., van Geldern, R., Freitag, H., Karim, A., Négrel, P., Petelet-Giraud, E., et al. (2011). Applications of stable water and carbon isotopes in watershed research:

weathering, carbon cycling, and water balances. *Earth Sci. Rev.* 109, 20–31. doi: 10.1016/j.earscirev.2011.07.003

Smith, C. A. S., Webb, K. T., Kenney, E., Anderson, A., and Kroetsch, D. (2011). Brunisolic soils of Canada: genesis, distribution, and classification. *Can. J. Soil Sci.* 91, 695–717. doi: 10.4141/cjss10058

Steinour, H. H. (1959). Some effects of carbon dioxide on mortars and concrete-discussion. *J. Am. Concrete Inst.* 30, 905–907.

Stubbs, A. R., Paulo, C., Power, I. M., Wang, B., Zeyen, N., and Wilson, S. A. (2022). Direct measurement of CO_2 drawdown in mine wastes and rock powders: implications for enhanced rock weathering. *Int. J. Greenhouse Gas Control* 113:103554. doi: 10.1016/j.ijggc.2021.103554

Sutherland, K., Matlin-Wainer, M., Holme, E., He, J., Savage, R., Marsland, E., et al. (2023). Enhanced weathering in agriculture v1.0 – isometric. 1–148. Available online at: https://registry.isometric.com/protocol/enhanced-weathering-agriculture (accessed March 10, 2024).

Swoboda, P., Döring, T. F., and Hamer, M. (2022). Remineralizing soils? The agricultural usage of silicate rock powders: a review. *Sci. Total Environ.* 807:150976. doi: 10.1016/j.scitotenv.2021.150976

Taylor, L. L., Driscoll, C. T., Groffman, P. M., Rau, G. H., Blum, J. D., and Beerling, D. J. (2021). Increased carbon capture by a silicate-treated forested watershed affected by acid deposition. *Biogeosciences* 18, 169–188. doi: 10.5194/bg-18-169-2021

te Pas, E. E. E. M., Hagens, M., and Comans, R. N. J. (2023). Assessment of the enhanced weathering potential of different silicate minerals to improve soil quality and sequester CO_2. *Front. Clim.* 4:954064. doi: 10.3389/fclim.2022.954064

ten Berge, H. F. M., van der Meer, H. G., Steenhuizen, J. W., Goedhart, P. W., Knops, P., and Verhagen, J. (2012). Olivine weathering in soil, and its effects on growth and nutrient uptake in ryegrass (Lolium perenne L.): a pot experiment. *PLoS One* 7:2098. doi: 10.1371/journal.pone.0042098

UNFCCC (2015). Paris Agreement. Paris: UNFCCC.

Vienne, A., Poblador, S., Portillo-Estrada, M., Hartmann, J., Ijiehon, S., Wade, P., et al. (2022). Enhanced weathering using basalt rock powder: carbon sequestration, co-benefits and risks in a mesocosm study with solanum tuberosum. *Front. Clim.* 4:869456. doi: 10.3389/fclim.2022.869456

Vink, J., Giesen, D., and Ahlrichs, E. (2022). Olivine weathering in field trials. Deltares technical report 11204378-000-BGS-0002, Utrecht.

Voigt, M., Marieni, C., Clark, D. E., Gíslason, S. R., and Oelkers, E. H.. (2018). Evaluation and refinement of thermodynamic databases for mineral carbonation. *Energy Procedia* 146, 81–91. doi: 10.1016/j.egypro.2018.07.012

Wang, B., Zeyen, N., Wilson, S., Honda-McNeil, M. J., Hamilton, J. L., Von Gunten, K., et al. (2024). Migration of transition metals and potential for carbon mineralization during acid leaching of processed kimberlite from Venetia diamond mine, South Africa. *Appl. Geochemistry* 166:105986. doi: 10.1016/j.apgeochem.2024.105986

Wani, O. B., Khan, S., Shoaib, M., Zeng, H., and Bobicki, E. R. (2022). Decarbonization of mineral processing operations: realizing the potential of carbon capture and utilization in the processing of ultramafic nickel ores. *Chem. Eng. J.* 433:134203. doi: 10.1016/j.cej.2021.134203

Webb, R. M. (2020). The law of enhanced weathering for carbon dioxide removal. Available online at: https://ssrn.com/abstract=3698944 (accessed May 6, 2024).

Weiler, J., Tassinari, C. C. G., De Aquino, T. F., Bonetti, B., and Viola, V. O. (2024). Using mining waste for CO_2 sequestration: exploring opportunities through mineral carbonation, nature-based solutions, and CCUS. *Int. J. Min. Reclam. Environ.* 38, 425–441. doi: 10.1080/17480930.2024.2318132

West, T. O., and McBride, A. C. (2005). The contribution of agricultural lime to carbon dioxide emissions in the United States: dissolution, transport, and net emissions. *Agric. Ecosyst. Environ.* 108, 145–154. doi: 10.1016/j.agee.2005.01.002

Wilson, S. A., Dipple, G. M., Power, I. M., Barker, S. L. L., Fallon, S. J., and Southam, G. (2011). Subarctic weathering of mineral wastes provides a sink for atmospheric CO_2. *Environ. Sci. Technol.* 45, 7727–7736. doi: 10.1021/es202112y

Wilson, S. A., Harrison, A. L., Dipple, G. M., Power, I. M., Barker, S. L. L., Ulrich Mayer, K., et al. (2014). Offsetting of CO_2 emissions by air capture in mine tailings at the mount Keith nickel mine, Western Australia: rates, controls and prospects for carbon neutral mining. *Int. J. Greenhouse Gas Control* 25, 121–140. doi: 10.1016/j.ijggc.2014.04.002

Wilson, S., Raudsepp, M., and Dipple, G. M. (2009). Quantifying carbon fixation in trace minerals from processed kimberlite: a comparative study of quantitative methods using X-ray powder diffraction data with applications to the Diavik diamond mine, Northwest Territories, Canada. *Appl. Geochem.* 24, 2312–2331. doi: 10.1016/j.apgeochem.2009.09.018

Wood, C., Harrison, A. L., and Power, I. M. (2023). Impacts of dissolved phosphorus and soil-mineral-fluid interactions on CO_2 removal through enhanced weathering of wollastonite in soils. *Appl. Geochem.* 148:105511. doi: 10.1016/j.apgeochem.2022.105511

Zeyen, N., Wang, B., Wilson, S. A., Paulo, C., Stubbs, A. R., Power, I. M., et al. (2022). Cation exchange in smectites as a new approach to mineral carbonation. *Front. Clim.* 4:913632. doi: 10.3389/fclim.2022.913632